Computational Study on the Dynamic Stability of a Blunt Reentry Capsule at Transonic Speeds

Susumu Teramoto

February, 2000

The Institute of Space and Astronautical Science

ABSTRACT

A flat capsule with blunt nose is often used for the reentry capsule of sample-return projects. It is known that such capsule tends to be dynamically unstable at transonic speeds. The instability phenomena has been studied experimentally since 1960's, but its mechanism is not well understood. The flowfield around the reentry capsule is numerically simulated and discussed to reveal the mechanism of the dynamic instability. A new post-processing technique that uses frequency filters, are applied to detect the flow structure out of complicated flowfield.

The results showed that the base pressure of the capsule produces pitch-down moment for the positive pitch angle, and the oscillation of the base pressure is delayed from the pitch angle when the capsule oscillates in pitch. The delay cause the hysteresis in the aerodynamic pitching moment, and the hysteresis makes the capsule dynamically unstable. The base pressure and the wake at the neck point (the foot of the recompression shock wave) oscillate with the same delay time. When the neck point moves upward, the pressure at the upper part of the base becomes higher and the base pressure produces pitch-down moment. Two oscillations coincides each other, and therefore the base pressure is correlated to the flowfield near the neck point.

There is strong reverse flow behind the capsule, and the impingement of the reverse flow against the base determine the base pressure distribution. The behavior of the reverse flow is governed by the vortex structure behind the capsule. The vortex is composed of the ring vortex and the pair of longitudinal vortices, and the interaction between the longitudinal vortices and the flowfield near the neck point define the base pressure

distribution. The base pressure does not change until the disturbance of the longitudinal vortices caused by the pitching motion of the capsule reaches the neck point, and the time lag is the cause of the phase delay of the base pressure.

Both the base pressure distribution and the delay of the base pressure is governed by the pair of longitudinal vortices, and therefore the dynamic stability of the capsule is closely related to the formation of the pair of longitudinal vortices.

ACKNOWLEDGMENT

This dissertation represents my research from the Summer of 1997 through the Spring of 2000 as a research associate of the Institute of Space and Astronautical Science.

I would like to express my best gratitude to Professor Kozo Fujii of the Institute of Space and Astronautical Science for his constant advises, suggestions and encouragement.

I would also like to thank Dr. Kouju Hiraki of the ISAS. He first pointed out the importance of the dynamic stability in the transonic speed range, and revealed many characteristic features of the phenomena through his experimental work. His work was the start point of my research, and the discussion with him was full of suggestion and very helpful.

Additional thanks are due to Professor Takashi Abe of the ISAS for clarifying discussions at the meeting.

Special thanks to the current and former members in Fujii's Lab. for supporting my research.

Susumu Teramoto

February, 2000

CONTENTS

LIST OF FIGURES

NOMENCLATURE

Roman Symbols

c : speed of sound

C_l : roll moment coefficient

C_L : lift coefficient

C_m : pitch moment coefficient

$C_{mq} + C_{m\dot{\alpha}}$: pitch damping coefficient

C_n : yaw moment coefficient

D : diameter of the capsule

e : total energy per unit volume

f : frequency

h : total enthalpy per unit volume

M : Mach number or pitch moment

p : static pressure

Pr : Prandtl number

q : angular velocity or dynamic pressure

Q : vector of the conservative variables

Re : Reynolds number

St : Strouhal number

t : time

u, v, w: velocity components

U, V, W: contravariant velocities

x, y, z: cartesian coordinate fixed to the object

Xe, Ye, Ze: cartesian coordinate fixed to the space

Greek Symbols

α : angle of attack

β : angle of sideslip

γ : specific heat ratio

Γ : circulation

δ : delay time

θ : pitch angle

μ : viscosity coefficient

ξ, η, ζ: generalized coordinate

ρ : density

ϕ : phase angle

ψ : roll angle

ω : angular velocity

Subscripts

b : base side

f : front side

l : laminar

t : turbulent

∞ : free stream

Superscripts

n : evaluated at nth time step

CHAPTER 1

INTRODUCTION

The sample-return project, which is the project to collect and return the sample of an extra-earth planet, is drawing attention recently. The Institute of Space and Astronautical Science (ISAS) started an asteroid sample-return project "Muses-C" in 1995[2] aiming at launch on 2002 and rendezvous with the asteroid "Nereus" on 2004. The collected sample will be returned by the reentry capsule separated from the mother spacecraft on 2006 [1]. The collected sample will bring us new knowledge about the origin and the evolution of the solar system, and the project is attractive from the scientific viewpoint. Besides, it is also a challenging theme for the engineering side as well, to design a spacecraft that meet the requirement of the mission.

One of the key issues for the engineering side is the development of the return capsule. A spacecraft returns from the interplanetary orbit usually decelerates using rocket engine before the reentry, and once enters the earth's orbit to keep the reentry velocity lower. However, since the weight of the return capsule is strictly restricted to enable such long range mission within limited launch capability, and the reentry capsule of the Muses-C depends on aerodynamic braking and it reenters directly from the hyperbolic earth-return trajectory to save the propellant required to transfer the orbit. Consequently, the nominal reentry velocity is expected to be 12 km/s which is much higher than that for the reentry from the earth's orbit, and severe heating is expected during the reentry. The capsule

[1]The project recently re-scheduled. The target asteroid is changed to 1989ML, and the launch is scheduled on the Summer of 2002

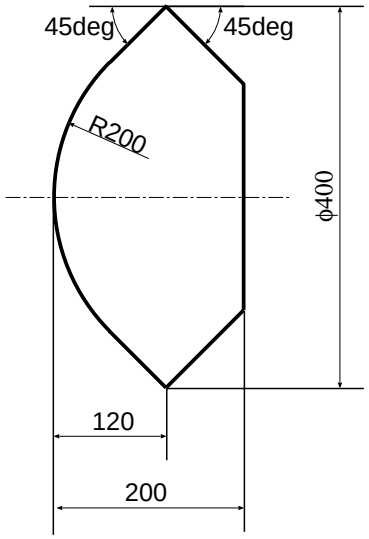

Figure 1.1: Outline configuration of the reentry capsule of the Muses-C

with small ballistic coefficient (large drag and light weight) experience large deceleration at the upper atmosphere where the convective heating is not severe, therefore lowering the ballistic coefficient reduce the maximum convective heating in general. Figure 1.1 shows the reentry capsule of the Muses-C. Large nose radius produce large drag, and short body length reduce the weight, resulting the small ballistic coefficient.

In addition to the heat protection, the attitude control of the capsule is also an important issue at the development of reentry capsules. The attitude of the vehicle must be maintained within the limit in the whole speed range, to protect the payload from strong heating in the hypersonic region, and to ensure the deployment of the parachute in the transonic and/or subsonic region. Since the capsule does not have any active attitude control device, the attitude of the capsule must be maintained by its own aerodynamic stability, and therefore the aerodynamic stability of the capsule is important for the design. Most of the basic configuration parameters such as nose radii or body lengths are determined mainly from the thermal protection requirement, and there are little room to optimize the configuration with respect to the aerodynamic stability. Fortunately, the center of gravity of such an capsule is located in forward of the center of pressure, and

the object is statically stable in general. However, such capsule tends to be dynamically unstable in the transonic speed range, and sometimes fall into self-exited pitching oscillation.

Since both the static and dynamic aerodynamic characteristics of reentry capsule have to be accurately determined for the feasibility study of the project, the dynamic stability of capsules are evaluated experimentally even in the early space developments, and the instability phenomenon at transonic speeds has been known since 1960's. The dynamic aerodynamic characteristics of the Gemini reentry capsule was measured by the one-dimensional forced oscillation method, and it was reported that the capsule was dynamically unstable around $\alpha = 180°$ (head shield forward) at low supersonic speeds[3]. The characteristics of the dynamic instability phenomena was studied intensively in conjunction with the Viking project. The aerodynamic characteristics of three candidate capsule configurations were evaluated by the ballistic range test facility[4]. Since the entry capsule of the Viking was required to have low ballistic coefficient, the three capsules were similar to the reentry capsule of Muses-C, and they were all dynamically unstable at transonic speeds. Sammonds [5] parametrically studied the dynamic stability of several blunted-cone capsules, and reported that a spherical afterbody with its center at the center of the gravity of the capsule eliminates the dynamic instability, while the corner radius of the capsule has no significant effect on its dynamic stability. The final configuration of Viking entry vehicle was also tested in the ballistic range, and the dynamic instability was confirmed for the Mach number around $M = 2$ and angle of attack $|\alpha| < 8°$ [6]. Yoshinaga[7] evaluated the pitch damping coefficient of the OREX, the first Japanese reentry vehicle, by the single-degree of freedom wind-tunnel experiment. The capsule fallen into self-excited oscillation at transonic speeds $0.95 < M < 1.5$, and the maximum amplitude of the oscillation exceeded $20°$ which was the mechanical limit of the model capsule. Yoshinaga reported that the amplitude of the sharp-edged capsule is smaller than that of the blunt-edged capsule. Berner[8] evaluated the static aerodynamic

coefficients of blunt capsules by a numerical simulation, and compared them with the experimental results obtained from the ballistic range test facility. He also evaluated the dynamic aerodynamic coefficients from the experiment, but there was no attempt to evaluate the dynamic characteristics of the capsule from the results of the numerical simulation. Chapman[9] reviewed the current state of the understandings on the aerodynamics of the blunt capsules, but there were no comments about the mechanism of the dynamic instability phenomena. In late 1990's, several reports about the dynamic stability of blunt capsules were published in conjunction with the Stardust, the comet sample return project in NASA. Chapman et al[10] investigated the pitch damping characteristics of the Stardust sample return capsule using ballistic range. The pitch damping of the capsule is highly nonlinear with the angle of attack; it was dynamically unstable at small angles of attack and dynamically stable at higher angles.

The dynamic stability of the capsules with particular configurations were studied one by one in these works, and there seemed to be little effort that reveals the mechanism of the dynamic instability. There is no way to evaluate the dynamic stability of a capsule before the experiment, and the dynamic stability of the capsule has been assured based on the trial-and-error approach in the design of reentry capsules. Several capsules have to be designed and tested iteratively until the optimized configuration is obtained, which is time and cost consuming work. If there is some guideline about the correlation between geometry of a capsule and its dynamic stability, it will greatly save the time and the cost to design capsules. The understandings of the mechanism of the dynamic instability is indispensable to establish such guideline. To the authors knowledge, it is Hiraki[1] who first tried to investigate the mechanism of the dynamic instability. Hiraki studied the dynamic stability of blunt capsules based on the wind tunnel experiment using a one-dimensional free-oscillation method, in conjunction with the Muses-C project. He discussed the instability phenomena in detail, and tried to reveal its mechanism.

Figure 1.2 shows his wind tunnel model. The model capsule is supported at its center

of the gravity by a bearing so that it rotates freely in the pitch. The capsule is first fixed at zero pitch angle, and released after the free stream is stabilized. Figures 1.3 show the time histories of the pitch angle after the release for various free stream Mach numbers. The capsule becomes dynamically unstable and falls into self excited oscillation with large amplitude at transonic speeds. The frequency of the limit cycle oscillation is approximately 20 Hz, and the reduced frequency is as low as $O(0.01)$. Hiraki modeled the motion of the capsule using curve fit technique. The model well agrees with the experimental results, and the model equation showed that the capsule is dynamically unstable for the small angle of attack, while it is dynamically stable for the large angle of attack. He also measured the time history of the surface pressure during the oscillation, and revealed that the base pressure plays an important role for the dynamic instability. The experiment was carried out with several capsule configurations, and he found that the dynamic stability of the capsule depends on its forebody shape. One model is dynamically unstable at transonic speeds, and the other model is dynamically stable for all speeds between $M = 0.3 \sim 2.5$. Hiraki concluded from the observation that the capsule with small semi-apex angle tends to be dynamically stable.

Hiraki's experiment revealed many interesting features about the dynamic instability of the capsule. However, his experimental data was limited to the history of the pitch angle and the surface pressure, and the influence of the sting is not evaluated while the influence of the base flowfield seems to be dominant for the dynamic instability phenomena. It is difficult to discuss the correlation between the flowfield and the dynamic stability only from these data in detail, and the mechanism of the dynamic stability is sill not clear. The objective of current study is to discuss the correlation between the flowfield and the dynamic stability, and reveal the mechanism of the dynamic stability phenomena at transonic speeds.

Typical dynamic instability is caused by the interaction between the oscillation of the attitude of the object and the oscillation of the flowfield, and if the oscillation of the

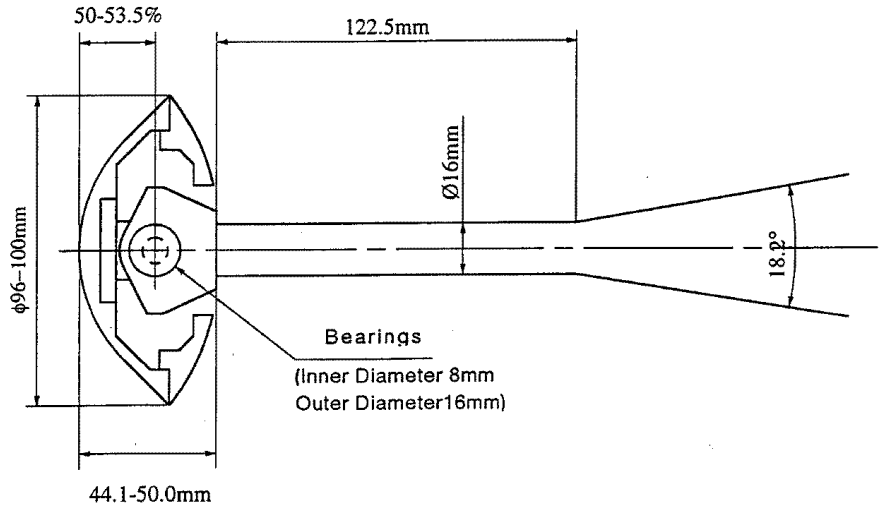

Figure 1.2: Wind tunnel model for one-dimensional free oscillation method (Ref.[1])

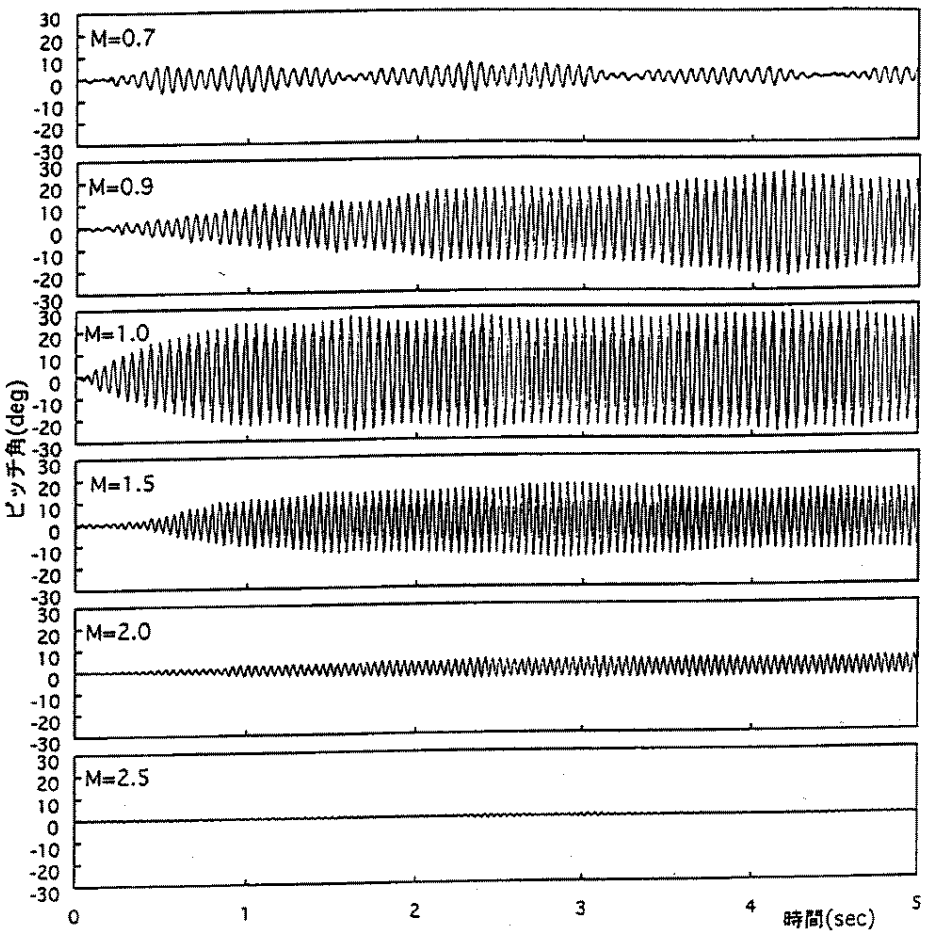

Figure 1.3: Time histories of pitch angle for various Mach numbers (Ref.[1])

flowfield that takes part in the dynamic instability is the oscillation which corresponds to the natural frequency (i.e. Strouhal number) of the flowfield, the reduced frequency of the limit cycle oscillation should be $O(1)$. Actual reduced frequency of the limit cycle oscillation observed in the experiment is as low as $O(0.01)$, and it seems that some flow structure which has longer length scale and/or lower characteristic speeds than the natural frequency oscillation, governs the dynamic instability phenomenon. Therefore, the information of the flowfield away from the body is essential for the discussion of the mechanism of the dynamic instability. From this view point, we choose the computational approach as it gives us the time-dependent information of the whole flowfield.

The contents of this dissertation are as follows.

Firstly, the modeling of the phenomena is discussed in chapter 2, and the description of the numerical methods used in this study is presented in chapter 3. Since the flowfield considered in this study is complicated, special attention is paid to the post processing of the numerical results. The flowfield around the capsule in the forced pitching oscillation is simulated and the temporal characteristic of the flowfield is discussed in chapter 4. The flowfield around the oscillating capsule and that around the capsule at fixed pitch angles are compared in chapter 5. The flowfield around the oscillating capsule is approximated by a simple constant-delay mode, and the characteristics of the dynamic stability of the capsule are discussed based on the model. The structure of the flowfield is investigated in detail from the simulation of the flowfield around the capsule at fixed pitch angles, and the correlation between the flowfield and the aerodynamic forces that work on the capsule is discussed in chapter 6. Finally, a model for the mechanism of the dynamic instability is proposed and validated in chapter7. The summary of the dissertation is presented in chapter 8.

CHAPTER 2

DEFINITION OF THE PROBLEM

The trajectory and the attitude of the capsule entering the atmosphere are influenced by its aerodynamic characteristics, the gravity and the density gradient along the path et cetera, and the capsule moves with six degrees of freedom. In this study, several assumptions are imposed for the motion of the capsule for the simplification of the analysis. Before going into the analysis, the assumptions and the definition of the problem considered in this study are described in this chapter.

2.1 Basic Assumptions

Firstly, following conditions are imposed.

- the center of the gravity of the capsule traverses a straight path with constant velocity
- the influence of the gravity is neglected
- the density of the atmosphere is constant along the flight path

There is no need to consider the translation of the center of the gravity under these conditions, and only the rotational motion about the center of the gravity is discussed hereafter.

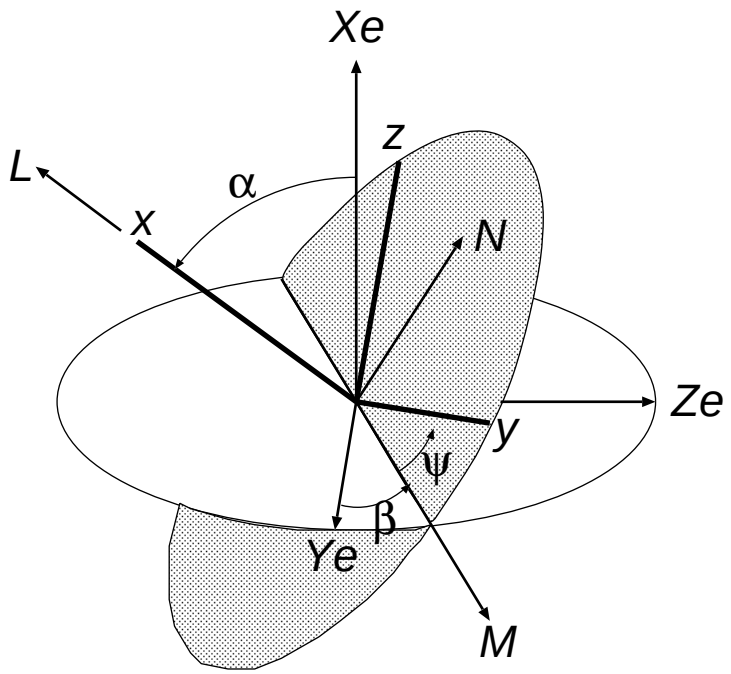

Figure 2.1: Coordinate system

2.2 Nonlinear Formulation of Aerodynamic Moment System

Figure 2.1 shows the definition of the coordinate system. Xe, Ye, Ze are the axes fixed to the space, and Xe is aligned to the direction of the uniform flow. x, y, z are the coordinate system fixed to the object where x is coincident with the axis of the symmetry of the object. The angle of attack α is the angle between the uniform flow and the axis of the symmetry, and the "pitching motion" is defined as the motion inside the α plane. The pitching moment M is the moment component normal to the α plane. Despite the basic assumptions, nonlinear effects and the coupling terms are not omitted at this step. Considering the axial symmetry of the object, the aerodynamic moments work upon the object are expressed as the functionals of the argument functions $\alpha(t)$,$\dot{\beta}(t)$ and $\dot{\psi}(t)$. Tobak et al[11] derived the simplified formulation of the aerodynamic moments from the

original functionals as follows

$$C_m(t) = C_m(\infty;\alpha(t)) + (\dot{\beta}l/V)C_{m\dot{\beta}}(\infty;\alpha(t)) + (\dot{\psi}l/V)C_{m\dot{\psi}}(\infty;\alpha(t)) + (\dot{\alpha}l/V)C_{m\dot{\alpha}}(\alpha(t)) \tag{2.1}$$

C_n, the yawing moment and C_l, the rolling moment are also expressed similarly.

The procedure to derive Eq. (2.1) is same as that presented in [12] and it is based on the following assumptions

- the flowfield does not changes drastically with α and q, and the terms higher than $(\Delta\alpha)^2$ $(\Delta q)^2$ are negligible
- the rate of the change of α is slow, and therefore $\dot{\alpha}$ is small
- the physical properties at certain moment depend only on the properties right before that moment

The flowfield considered in this study is the flow around the object with simple geometry. The separation point is fixed the edge of the capsule, and the flowfield does not change drastically with the pitch angle. The motion of the object is so slow that the reduced frequency is as low as $O(0.01)$. Therefore, all these assumptions are convincing.

The third term in Eq. (2.1) is the Magnus moment caused by the rolling angular velocity $\dot{\psi}$. The history of the attitude of the OREX during the actual reentry [7] show that the period of the rolling is one order of the magnitude longer than that of the pitching oscillation, and therefore the Magnus moment is considered to be negligible. The second term in Eq. (2.1) is the pitching moment caused by the coning motion. Considering the axial symmetry of the capsule, the contribution of the second term is also considered to be small. The formulation of the aerodynamic moments finally reduce to the following [11]:

$$C_m(t) \;=\; C_m(\infty;\alpha(t)) + (\dot{\alpha}l/V)C_{m\dot{\alpha}}(\alpha(t)) \tag{2.2}$$

$$C_n(t) = (\dot{\beta}l/V)C_{n\dot{\beta}}(\infty;\alpha(t)) \tag{2.3}$$

Note that the conditions imposed to derive Eqs. (2.2) and (2.3) are

- three basic assumptions
- three assumptions to derive Eq. (2.1)
- the experimental result that the rolling rate is low
- the object is axially symmetric and the coning motion of the object produce a small pitching moment

which are all considered to be reasonable for the problem considered in this dissertation.

Equations (2.2) and (2.3) show that even when the capsule oscillates with all three motions, pitching, rolling and coning in reality, the pitch stability of the capsule can be discussed from the analysis of the planer pitching oscillation.

2.3 Modeling of the Phenomena

Based on the above discussions, the planer pitching oscillation of the capsule is studied in this dissertation. The capsules used in the present study are those used in the Hiraki's experiment. Figures 2.2 and 2.3 show two capsules used in the Hiraki's experiment. The geometric parameters of the capsules are listed in Table 2.1. The wind tunnel experiment showed that the D45 model is dynamically unstable at transonic speeds, and the D30 model is dynamically stable for all speeds between $M = 0.3 \sim 2.5$. Since the gravity is neglected from the basic assumption, there is arbitrariness in the selection of the α plane, and the α plane is selected to be the perpendicular plane.

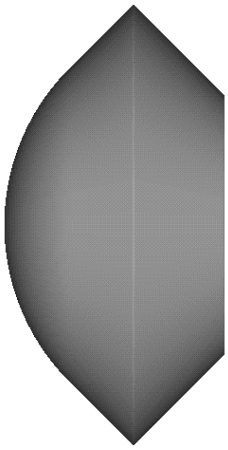

Figure 2.2: D45 model capsule

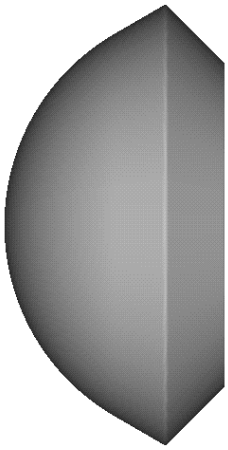

Figure 2.3: D30 model capsule

Table 2.1: Geometry of the model capsules

	D45 Model	D30 Model
nose radius	50 mm	
semi-apex angle	45 degree	30 degree
maximum diameter	100 mm	
body length	50 mm	
base configuration	45 degree truncated cone	
dynamic stability at transonic speeds	unstable	stable

CHAPTER 3

NUMERICAL METHODS

3.1 Flow Solver

3.1.1 Governing Equations

The governing equations are the three-dimensional Navier-Stokes equations. Physical properties are non-dimensionalized by the speed of sound and the density of the uniform flow, and the length is non-dimensionalized by the diameter of the capsule. The concrete formulation of the Navier-Stokes equations and the non-dimensionalization are given in Appendix A.

The equations are discretized and solved by the finite difference method on a discrete grid system. Since the numerical dissipation accompanied with the spatial discretization is proportional to the grid spacing, the grid has to be clustered at the region where the viscous effect is dominant to resolve the viscous layer. Otherwise, excessive numerical dissipation mask the physical viscous term and the profile of the viscous layer is determined mainly by the grid distribution no matter how the physical viscous term is included in the governing equations. As for the flowfield considered in this study, viscous effect is dominant at the boundary layer near the capsule and the shear layer at the edge of the wake downstream. It is not difficult to cluster the grid at the wall to resolve the boundary layer. However, the location of the shear layer is not known before the simulation, and it is almost impossible to cluster the grid at the shear layer within practical number

of total grid points. Fortunately, the difference in the profile of the shear layer at the wake does not change the large scale structure of the flowfield in many cases. Hiraki's experimental result indicates that the dynamic instability phenomena considered in this study is governed by the flow structure which has long length scale, and therefore even the simulation that neglect the physical viscous effect at the shear layer downstream will provide useful information for the qualitative discussion about the instability phenomena. The "thin-layer approximation" is applied to the viscous terms, and the spatial derivatives parallel to the wall ($\frac{\partial}{\partial \xi}$ and $\frac{\partial}{\partial \eta}$) are omitted. The equations are transformed to the generalized curvilinear coordinate system as follows.

$$\frac{\partial \hat{Q}}{\partial t} + \frac{\partial \hat{E}}{\partial \xi} + \frac{\partial \hat{F}}{\partial \eta} + \frac{\partial \hat{G}}{\partial \zeta} = Re^{-1}\frac{\partial \hat{S}}{\partial \zeta} \tag{3.1}$$

$$\hat{Q} = J^{-1}\begin{bmatrix} \rho \\ \rho u \\ \rho v \\ \rho w \\ e \end{bmatrix}, \quad \hat{E} = J^{-1}\begin{bmatrix} \rho U \\ \rho u U + \xi_x p \\ \rho v U + \xi_y p \\ \rho w U + \xi_z p \\ U(e+p) - \xi_t p \end{bmatrix}, \quad \hat{F} = J^{-1}\begin{bmatrix} \rho V \\ \rho u V + \eta_x p \\ \rho v V + \eta_y p \\ \rho w V + \eta_z p \\ V(e+p) - \eta_t p \end{bmatrix}$$

$$\hat{G} = J^{-1}\begin{bmatrix} \rho W \\ \rho u W + \zeta_x p \\ \rho v W + \zeta_y p \\ \rho w W + \zeta_z p \\ W(e+p) - \zeta_t p \end{bmatrix}, \quad \hat{S} = J^{-1}\begin{bmatrix} 0 \\ \mu m_1 u_\zeta + (\mu/3) m_2 \zeta_x \\ \mu m_1 v_\zeta + (\mu/3) m_2 \zeta_y \\ \mu m_1 w_\zeta + (\mu/3) m_2 \zeta_z \\ \mu m_1 m_3 + (\mu/3) m_2 (\zeta_x u + \zeta_y v + \zeta_z w) \end{bmatrix}$$

$$p = (\gamma - 1)\left\{ e - \frac{1}{2}\rho\left(u^2 + v^2 + w^2\right)\right\}$$

$$\begin{aligned} m_1 &= \zeta_x{}^2 + \zeta_y{}^2 + \zeta_z{}^2 \\ m_2 &= \zeta_x u_\zeta + \zeta_y v_\zeta + \zeta_z w_\zeta \end{aligned}$$

$$m_3 = \frac{1}{2}(u^2+v^2+w^2)_\zeta + \frac{1}{Pr(\gamma-1)}(c^2)_\zeta$$

For the turbulent simulation, μ and Pr are replaced by

$$\mu = \mu_l + \mu_t, \qquad \frac{\mu}{Pr} = \frac{\mu_l}{Pr_l} + \frac{\mu_t}{Pr_t}$$

The turbulent eddy viscosity coefficient μ_t is evaluated from a turbulence model. U, V and W are the contravariant velocities

$$\begin{aligned} U &= \xi_t + \xi_x u + \xi_y v + \xi_z w \\ V &= \eta_t + \eta_x u + \eta_y v + \eta_z w \\ W &= \zeta_t + \zeta_x u + \zeta_y v + \zeta_z w \end{aligned}$$

Since the grid system moves with the capsule, the components correspond to the translation of the grid points are added to the conventional definitions of the contravariant velocities. Metrics and jacobian are given as follows

$$\begin{aligned} \xi_x &= J(y_\eta z_\zeta - z_\eta y_\zeta), \quad \xi_y = J(z_\eta x_\zeta - x_\eta z_\zeta), \quad \xi_z = J(x_\eta y_\zeta - y_\eta x_\zeta) \\ \eta_x &= J(y_\xi z_\zeta - z_\xi y_\zeta), \quad \eta_y = J(z_\xi x_\zeta - x_\xi z_\zeta), \quad \eta_z = J(x_\xi y_\zeta - y_\xi x_\zeta) \\ \zeta_x &= J(y_\xi z_\eta - z_\xi y_\eta), \quad \zeta_y = J(z_\xi x_\eta - x_\xi z_\eta), \quad \zeta_z = J(x_\xi y_\eta - y_\xi x_\eta) \end{aligned}$$

$$\begin{aligned} \xi_t &= -(\xi_x x_\tau + \xi_y y_\tau + \xi_z z_\tau) \\ \eta_t &= -(\eta_x x_\tau + \eta_y y_\tau + \eta_z z_\tau) \\ \zeta_t &= -(\zeta_x x_\tau + \zeta_y y_\tau + \zeta_z z_\tau) \end{aligned}$$

$\xi_{x,y,z}$,$\eta_{x,y,z}$ and $\zeta_{x,y,z}$ correspond to the area vector of the cell interface, and ξ_t,η_t and ζ_t represent the volume being swept by the translation of the cell interface. Since the

grid rotates with time, these metrics are evaluated every time step. The grid does not deform, and therefore the jacobian is constant with time.

$$J^{-1} = x_\xi y_\eta z_\zeta + x_\eta y_\zeta z_\xi + x_\zeta y_\xi z_\eta - x_\xi y_\zeta z_\eta - x_\eta y_\xi z_\zeta - x_\zeta y_\eta z_\xi$$

The flowfield considered in this study is transonic. The static temperature does not changes much from the reference value, and the laminar viscosity μ_l is assumed to be constant for the whole flowfield.

3.1.2 General discretization

Partial differential equation (3.1) is discretized as follow

$$\hat{Q}^{n+1}_{j,k,l} = \hat{Q}^n_{j,k,l} + \left(\lambda R(\hat{Q}^{n+1}) + (1-\lambda)R(\hat{Q}^n)\right) \tag{3.2}$$

$$\begin{aligned} R(\hat{Q}^n) = -\Delta t \Big(&\tilde{E}_{j+\frac{1}{2},k,l} - \tilde{E}_{j-\frac{1}{2},k,l} + \tilde{F}_{j,k+\frac{1}{2},l} - \tilde{F}_{j,k-\frac{1}{2},l} + \tilde{G}_{j,k,l+\frac{1}{2}} - \tilde{G}_{j,k,l-\frac{1}{2}} \\ &+\tilde{S}_{j,k,l+\frac{1}{2}} - \tilde{S}_{j,k,l-\frac{1}{2}}\Big)^n \end{aligned} \tag{3.3}$$

Here, temporal difference of the conservative variable $\hat{Q}$ is evaluated by the trapezoidal method, and the spatial differences of the flux $\hat{E}, \hat{F}, \hat{G}$ are evaluated by the central difference. $\tilde{E}, \tilde{F}$ and $\tilde{G}$ are the numerical fluxes defined at the cell interface. The temporal accuracy of the scheme varies with the λ. $\lambda = 0$ yields first-order Euler explicit scheme, $\lambda = \frac{1}{2}$ yields Crank-Nicolson second-order implicit scheme, and $\lambda = 1$ gives first-order Euler implicit scheme. The spatial accuracy depends mainly on the evaluation of the numerical fluxes.

3.1.3 Evaluation of Numerical Fluxes

Roe's Flux Differences Scheme[13] is widely used for the numerical fluxes in the simulation of transonic flowfields. Roe's scheme gives good resolution of both the shock wave and

the boundary layer, and it is suitable for the simulation of transonic viscous flowfield. This scheme is, however, less robust and suffers from numerical instability at the strong expansion which is observed at the edge of the reentry capsule. In the present study, the numerical fluxes are evaluated by the SHUS (Simple High-resolution Upwind Scheme) scheme[14] which is a family of the AUSM[15] type schemes, to avoid numerical instability at the strong expansion while maintain the resolution of the shock wave and the boundary layer.

The AUSM scheme splits the numerical flux into two part, one from the contribution of the *convective term*, and the other from the *pressure term* as follows

$$E_{j+\frac{1}{2}} = \begin{pmatrix} \rho \\ \rho u \\ \rho v \\ \rho w \\ e \end{pmatrix} u_{j+\frac{1}{2}} + \begin{pmatrix} 0 \\ p_{j+\frac{1}{2}} \\ 0 \\ 0 \\ 0 \end{pmatrix} = E^{(c)}_{j+\frac{1}{2}} + \begin{pmatrix} 0 \\ p_{j+\frac{1}{2}} \\ 0 \\ 0 \\ 0 \end{pmatrix} \tag{3.4}$$

convective term represents the scalar physical properties transported by the mass flux ρu, therefore it is evaluated by the upwind differencing

$$E^{(c)}_{j+\frac{1}{2}} = u_{j+\frac{1}{2}} \begin{pmatrix} \rho \\ \rho u \\ \rho v \\ \rho w \\ e \end{pmatrix}_{j+\frac{1}{2}} = M_{j+\frac{1}{2}} \begin{pmatrix} \rho c \\ \rho c u \\ \rho c v \\ \rho c w \\ \rho c h \end{pmatrix}_{j+\frac{1}{2}}$$

$$= M_{j+\frac{1}{2}} \begin{pmatrix} \rho c \\ \rho cu \\ \rho cv \\ \rho cw \\ \rho ch \end{pmatrix}_L \text{if } M_{j+\frac{1}{2}} \geq 0, \quad M_{j+\frac{1}{2}} \begin{pmatrix} \rho c \\ \rho cu \\ \rho cv \\ \rho cw \\ \rho ch \end{pmatrix}_R \text{if } M_{j+\frac{1}{2}} < 0 \tag{3.5}$$

where subscripts L and R denote the physical states at the left and right side of the cell interface respectively. $M_{j+\frac{1}{2}}$ and $p_{j+\frac{1}{2}}$ are defined as follows

$$M_{j+\frac{1}{2}} = M_L^+ + M_R^-, \qquad M^{\pm} = \begin{cases} \pm\frac{1}{4}(M \pm 1)^2, & \text{if } |M| \leq 1; \\ \frac{1}{2}(M \pm |M|), & \text{otherwise} \end{cases} \tag{3.6}$$

$$p_{j+\frac{1}{2}} = p_L^+ + p_R^-, \qquad p^{\pm} = \begin{cases} \frac{p}{4}(M \pm 1)^2(2 \mp M), & \text{if } |M| \leq 1; \\ \frac{p}{2}(M \pm |M|)/M, & \text{otherwise} \end{cases} \tag{3.7}$$

Shima and Jounouchi[14] rewrote Eqs (3.4) to (3.7) into generalized formulation.

$$E_{j+\frac{1}{2}} = \frac{m + |m|}{2}\Phi_+ + \frac{m - |m|}{2}\Phi_- + \tilde{p}N \tag{3.8}$$

$$\Phi = \begin{pmatrix} 1 \\ u \\ v \\ w \\ h \end{pmatrix}, \qquad N = \begin{pmatrix} 0 \\ 1 \\ 0 \\ 0 \\ 0 \end{pmatrix}, \qquad m = \rho u, \qquad \tilde{p} = \beta_+ p_+ + \beta_- p_-$$

$$\beta_{\pm} = \begin{cases} \frac{1}{4}(2 \mp M_{\pm})(M_{\pm} \pm 1)^2, & \text{if } |M \pm| \leq 1 \\ \frac{1}{2}(M \pm |M|)/M, & \text{otherwise} \end{cases}$$

where subscripts $\pm$ denote the left and right side of the cell interface. They showed that all the AUSM type schemes such as original AUSM, AUSM$^+$, AUSMDV, SFS and

SHUS can be expressed by this formulation. The difference between these schemes is the expression of the mass flux m. SHUS scheme uses the mass flux of an approximate Riemann flux for the mass flux m.

$$m = \frac{1}{2}\left\{(\rho u)_+ + (\rho u)_- - |\bar{u}|\Delta\rho - \frac{|\bar{M}+1| - |\bar{M}-1|}{2}\bar{\rho}\Delta u \right. \\ \left. - \frac{|\bar{M}+1| + |\bar{M}-1| - 2|\bar{M}|}{2}\frac{\Delta p}{\bar{c}}\right\} \tag{3.9}$$

$$\Delta\rho = \rho_- - \rho_+, \quad \Delta p = p_- - p_+, \quad \Delta u = u_- - u_+$$

$$\bar{\rho} = \frac{\rho_+ + \rho_-}{2}, \quad \bar{p} = \frac{p_+ + p_-}{2}, \quad \bar{u} = \frac{u_+ + u_-}{2}, \quad \bar{c} = \sqrt{\gamma\frac{\bar{p}}{\bar{\rho}}}, \quad \bar{M} = \frac{\bar{u}}{\bar{c}}$$

The experience showed that the SHUS scheme is rather robust and efficient than the Roe's flux difference splitting.

The physical properties at the both sides of the interface, Q_+ and Q_- are evaluated by the MUSCL (Monotone Upstream-centered Schemes for Conservation Law) interpolation based on the primitive variables with the differentiable limiter. [16]

$$Q^+_{j+\frac{1}{2}} = Q_j + \left\{\frac{s}{4}\left[(1-\kappa s)\,\Delta_- + (1+\kappa s)\,\Delta_+\right]\right\}_j \tag{3.10}$$

$$Q^-_{j+\frac{1}{2}} = Q_{j+1} - \left\{\frac{s}{4}\left[(1-\kappa s)\,\Delta_+ + (1+\kappa s)\,\Delta_-\right]\right\}_{j+1} \tag{3.11}$$

$$s = \frac{2\Delta_+\Delta_- + \varepsilon}{(\Delta_+)^2 + (\Delta_-)^2 + \varepsilon}$$

$$(\Delta_+)_j \equiv Q_{j+1} - Q_j, \qquad (\Delta_-)_j \equiv Q_j - Q_{j-1}$$

The spatial accuracy of the scheme varies with the value of κ. $\kappa = +1$ yields second-order central difference scheme, $\kappa = -1$ to second-order fully-upwind scheme, and $\kappa = \frac{1}{3}$ gives upwind-biased third-order scheme. κ is set to be $\frac{1}{3}$ in the present study. ε is a small number (typically 10^{-6}) to prevent division by zero at the uniform region where $\Delta_+ = \Delta_- = 0$

3.1.4 Time Integration

The flowfield considered in this study is essentially unsteady, and the numerical scheme which has higher temporal accuracy is preferable for the discussion of the temporal behavior of the flowfield. In addition to the temporal accuracy, total simulation time (time step $\Delta t\times$ total iteration number) is also important since the time scale of the phenomenon is very long. Therefore, the numerical scheme have to be numerically efficient so that the simulation of long total simulation time is carried out within allowable wall clock time. The selection of the time integration scheme is the trade-off between the time accuracy, total simulation time, and the wall clock time required for the simulation.

The explicit time marching method is one choice. Even the simplest Euler explicit scheme has at least first-order temporal accuracy, and it is easy to extend temporal accuracy of the explicit schemes using the Runge-Kutta method. However, the time step Δt for the explicit schemes is restricted by the CFL condition, and the restriction is so strict when the grid is clustered near the wall to resolve the boundary layer, that it is almost impossible to simulate the phenomena which have long time scale. The LU-ADI factorization implicit algorithm[17] with no inner iteration is used for the time integration in this study to overcome the restriction of the time step Δt.

Let $\lambda = 1$ and rewrite Eqs. (3.2) and (3.3),

$$\Delta\hat{Q}^n \equiv \hat{Q}^{n+1} - \hat{Q}^n = -\Delta t \left(\partial_\xi \tilde{E} + \partial_\eta \tilde{F} + \partial_\zeta \tilde{G}\right)^{n+1} \tag{3.12}$$

note that the viscous terms are omitted for simplicity. Then locally linearize the numerical fluxes and Eq. (3.12) reduces to

$$\Delta\hat{Q}^n = -\Delta t \left(\partial_\xi \left(\tilde{E} + \hat{A}\Delta\hat{Q}\right) + \partial_\eta \left(\tilde{F} + \hat{B}\Delta\hat{Q}\right) + \partial_\zeta \left(\tilde{G} + \hat{C}\Delta\hat{Q}\right)\right)^n \tag{3.13}$$

$$\left[I + \Delta t \left(\delta_\xi \hat{A} + \delta_\eta \hat{B} + \delta_\zeta \hat{C}\right)\right] \Delta\hat{Q}^n = -\Delta t \left(\partial_\xi \tilde{E} + \partial_\eta \tilde{F} + \partial_\zeta \tilde{G}\right)^n \equiv R.H.S. \tag{3.14}$$

where δ_ξ, δ_η and δ_ζ are the finite difference operator for each direction, and $\hat{A}, \hat{B}$ and $\hat{C}$ are the jacobian matrix of the numerical fluxes

$$\hat{A} = \frac{\partial \tilde{E}}{\partial \hat{Q}}, \qquad \hat{B} = \frac{\partial \tilde{F}}{\partial \hat{Q}}, \qquad \hat{C} = \frac{\partial \tilde{G}}{\partial \hat{Q}}$$

The implicit operator inside the [ ] of the left hand side of Eq. (3.14) is the 5×5 sparse but non-band block matrix, and it is a tough work to inverse it. Equation (3.14) is further approximated and decomposed into the factorized form.

$$\left[I + \Delta t \delta_\xi \hat{A}\right] \left[I + \Delta t \delta_\eta \hat{B}\right] \left[I + \Delta t \delta_\zeta \hat{C}\right] \Delta \hat{Q}^n = R.H.S \tag{3.15}$$

Now, each implicit operator reduces to 5×5 tri-diagonal block matrix when the finite difference operator δ is evaluated by the second-order central difference. Each implicit operator can be written in the diagonal form:

$$\left[I + \Delta t \delta_\xi \hat{A}\right] \doteq R_\xi \left(I + \Delta t \delta_\xi \Lambda_\xi\right) R_\xi^{-1} \tag{3.16}$$

where R_ξ and Λ_ξ are the matrix of the right eigen vectors and the vector of the eigen values of the jacobian matrix $\hat{A}$. Here, $\hat{A} = R_\xi \Lambda_\xi R_\xi^{-1}$. Then eigen value Λ_ξ split into positive and negative components.

$$\left[I + \Delta t \delta_\xi \hat{A}\right] = R_\xi \left(I + \Delta t \delta_\xi \Lambda_\xi^+ + \Delta t \delta_\xi \Lambda_\xi^-\right) R_\xi^{-1} \tag{3.17}$$

$$\Lambda_\xi^\pm = \frac{1}{2}\left(\Lambda_\xi + |\Lambda_\xi|\right)$$

Introducing the idea of the flux vector splitting schemes, the difference operator δ_ξ for the positive components Λ_ξ^+ is evaluated by one-sided backward differencing, and the operator for the negative component Λ_ξ^- is evaluated by one-sided forward differencing.

The implicit operator for ξ-direction finally yields

$$\begin{aligned}\left[I + \Delta t \delta_\xi \hat{A}\right] &= R_\xi \left(I + \Delta t \delta_\xi^b \Lambda_\xi^+ + \Delta t \delta_\xi^f \Lambda_\xi^-\right) R_\xi^{-1} \\ &= R_\xi \left(I - \Delta t \Lambda_{\xi_j}^- + \Delta t \delta_\xi^b \Lambda_\xi^+\right) \left(I + \Delta t \left|\Lambda_\xi\right|\right)^{-1} \\ &\quad \left(I + \Delta t \Lambda_{\xi_j}^+ + \Delta t \delta_\xi^f \Lambda_\xi^-\right) R_\xi^{-1} \end{aligned} \tag{3.18}$$

note that $\Lambda_\xi^+ + \Lambda_\xi^- = |\Lambda_\xi|$.

Implicit operators for η- and ζ-direction are also decomposed similarly. The sparse 5×5 block matrix in Eq. (3.14) finally reduces to the product of 5×5 block diagonal matrix, scalar diagonal matrix, and lower and upper scalar bi-diagonal matrixes. The inversion of the final implicit operator does not require any matrix inversion, and the LU-ADI scheme is very efficient. The LU-ADI scheme introduces several approximation to inverse the implicit operator efficiently, and its temporal accuracy is less than first-order. However, according to Imai's study[18], the LU-ADI scheme has sufficient temporal accuracy to resolve the behavior of large scale vortex structure provided that the local CFL number is smaller than unity in the inviscid region. [1]

The grid spacing and the time step are carefully chosen in the present study, to maintain time accuracy enough to resolve the temporal behavior of the flowfield.

3.1.5 Turbulence Model

The turbulent viscosity μ_t is evaluated from the Baldwin-Lomax algebraic eddy-viscosity model[19]. This model was developed for the two-dimensional attached and steady boundary layer, and it evaluates the turbulent viscosity from the velocity profile along the line "normal" to the wall. There has been a lot of discussions about the use of Baldwin-Lomax turbulence model for the unsteady simulation of the three-dimensional separated flowfield. However, the separation point is clearly fixed to the edge of the capsule in this

[1] The summary of Imai's study is presented in Appendix B.

case, and the turbulence model does not seem to influence the qualitative mechanism of the flowfield. Therefore, one of the simplest turbulence model is used to reduce the computational cost.

The turbulent viscosity μ_t is given by

$$\mu_t = \begin{cases} (\mu_t)_{inner}, & y \leq y_{crossover}; \\ (\mu_t)_{outer}, & \text{otherwise} \end{cases} \tag{3.19}$$

where y is the normal distance from the wall, and $y_{crossover}$ is the smallest y at which $(\mu_t)_{inner}$ and $(\mu_t)_{outer}$ are equal. $(\mu_t)_{inner}$ is the turbulent viscosity inside the inner layer, and it is given by

$$(\mu_t)_{inner} = \rho l^2 |\omega|, \qquad l = ky\left[1 - \exp(-y^+/A^+)\right] \tag{3.20}$$

where $|\omega|$ is the magnitude of the vorticity, and y^+ is defined as

$$y^+ = \frac{\sqrt{\rho_w \tau_w}}{\mu_w} y \tag{3.21}$$

the subscript w denotes the properties evaluated at the wall, and τ_w is the skin friction at the wall. The turbulent viscosity at the outer region $(\mu_t)_{outer}$ is given by

$$(\mu_t)_{outer} = K\, C_{CP}\, \rho\, F_{WAKE}\, F_{KLEB}(y) \tag{3.22}$$

$$F_{WAKE} = min\left(y_{max}\, F_{max}, \quad C_{WK}\, y_{max}\, u_{DIF}^2\, F_{max}\right) \tag{3.23}$$

F_{max} is the maximum value of the function $F(y)$ along the line normal to the wall, and y_{max} is the y at which $F(y)$ takes its maximum value. The function $F(y)$ is defined as follows

$$F(y) = y|\omega|\left[1 - \exp(-y^+/A^+)\right] \tag{3.24}$$

F_{KLEB} is the Klebanoff intermittency factor given by

$$F_{KLEB}(y) = \left[1 + 5.5\left(\frac{C_{KLEB}\, y}{y_{max}}\right)^6\right]^{-1} \tag{3.25}$$

The constants appear in the equations are given as follows.

$$A^+ = 26, \qquad C_{CP} = 1.6, \qquad C_{KLEB} = 0.3, \qquad C_{WK} = 0.25$$

$$k = 0.4, \qquad K = 0.0168, \qquad Pr = 0.72, \qquad Pr_t = 0.9$$

For the flowfield with an attached boundary layer, magnitude of the vorticity $|\omega|$ outside the boundary layer is small. The function $F(y)$ takes its maximum at the edge of the boundary layer, therefore the y_{max} represents the thickness of the boundary layer. However, when strong shear layer exists away from the wall, another peak of $|\omega|$ appears at the shear layer, and $F(y)$ may take its maximum there. In such cases, y_{max} becomes far larger than the boundary layer thickness, and it makes $(\mu_t)_{outer}$ too large. The local maxima of $F(y)$ at the edge of the boundary layer has to be distinguished from other peaks caused by the large vorticity outside the boundary layer, to evaluate the turbulent viscosity of the separated flowfield properly. In this study, the F_{max} and y_{max} are searched from the region within prescribed distance ($\delta/D < 0.013$ for the front side, $\delta/D < 0.028$ for the base side) from the wall.

3.1.6 Boundary Conditions

Solid Wall Boundary

Solid wall boundary at the surface of the capsule is treated as "non-slip" wall, and the velocity components at the wall are given as

$$u = x_\tau, \quad v = y_\tau, \quad w = z_\tau \tag{3.26}$$

where x_τ, y_τ, z_τ are the velocities of the grid point at the wall. The density is extrapolated from the adjacent node.

$$\rho_{l=1} = \rho_{l=2}$$

The pressure is defined from the equilibrium condition of the momentum normal to the wall ("normal momentum equation")

$$\frac{\partial p}{\partial n} = -\rho \frac{u_{||}^2}{R} \tag{3.27}$$

where n is the unit vector normal to the wall, $u_{||}$ is the velocity component parallel to the wall, and R is the radius of the curvature of the wall. Equation (3.27) is expressed in the generalized coordinate system as follows:

$$Ap_\xi + Bp_\eta + p_\zeta = C \tag{3.28}$$

$$\begin{cases} A &= \frac{1}{D}\left(\xi_x\zeta_x + \xi_y\zeta_y + \xi_z\zeta_z\right) \\ B &= \frac{1}{D}\left(\eta_x\zeta_x + \eta_y\zeta_y + \eta_z\zeta_z\right) \\ C &= \frac{1}{D}\left\{\rho U\left(\xi_x\zeta_x + \xi_y\zeta_y + \xi_z\zeta_z\right) + \rho V\left(\eta_x\zeta_x + \eta_y\zeta_y + \eta_z\zeta_z\right)\right\} \\ D &= \zeta_x^2 + \zeta_y^2 + \zeta_z^2 \end{cases}$$

here, the wall is $\zeta = const$ plane.

Outer Boundary

The physical properties at the outer boundary are fixed to those of the uniform flow.

$$Q_{l=l_{max}} = Q_\infty$$

Periodic Boundary

The nodes at planes $k = 1, 2, 3$ and $k = 4$ are coincident with the nodes at planes $k = k_{max} - 3, k_{max} - 2, k_{max} - 1$ and $k = k_{max}$ respectively. Therefore,

$$Q_{k=1} = Q_{k=k_{max}-3} \quad , \qquad Q_{k=2} = Q_{k=k_{max}-2}$$

$$Q_{k=k_{max}-1} = Q_{k=3} \quad , \qquad Q_{k=k_{max}} = Q_{k=4}$$

Axis Singularity

The properties along the singular line at the axis is averaged from the variables at the nodes around the axis.

$$Q_{j=1,j_{max}} = \frac{1}{k_{max} - 4} \sum_{k=2}^{k_{max}-3} Q_{j,k}$$

3.2 Data Processing

The flow configuration considered in this study, such as the shape of the object or the flow conditions, are relatively simple. However, resultant flowfield is rather complicated and shows unique characteristics.

The frequency of the oscillation of the capsule is 20 Hz. The reduced frequency is as low as $O(0.01)$, and the variation of the flowfield due to the pitching motion of the capsule is very slow. On the other hand, there is a shedding of vortex, which is analogous to the Karman vortex, behind the capsule. The Strouhal number is $O(1)$ and the frequency of the shedding is a few kHz, which is much higher than the frequency of the pitching oscillation of the capsule. Since we are interested in the "slow" pitching oscillation of the capsule, the purpose of the post processing is to derive information that is related to the slow variation of the flowfield from the results of the simulation. Animations are commonly used for the analysis of the unsteady flow simulations. However, there are several difficulty in observing the "slow" phenomena only by simple animations:

- The unsteady evolution of the flowfield have to be simulated during at least several oscillation cycles, while the interval at which the flow variable are saved to files, have to be small enough to resolve the highest frequency of the flowfield. Therefore, many (typically more than one thousand files, tens gigabytes in size) data has to be processed for the discussion of the unsteady flowfield.

- The reduced frequency of the oscillation is very small, and the influence of the pitching motion of the capsule upon the flowfield is very small. Weak variation of the flowfield has to be distinguished out of the disturbed flowfield.

Following two methods are applied in the data processing to derive information out of the complicated results of the present simulation.

3.2.1 Curve Fitting

The discrete time series of the flow properties are approximated by the superposition of harmonic oscillations.

$$Q^n \approx \frac{1}{2}a_0 + \sum_{k=0}^{N} a_k \cos\left(k\omega\left(n\Delta t\right)\right) + \sum_{k=0}^{N} b_k \sin\left(k\omega\left(n\Delta t\right)\right) \tag{3.29}$$

where a_k, b_k are the amplitude for kth harmonic component, and $\omega = 2\pi f$ is the angular velocity of the pitching oscillation of the capsule. The amplitudes a_k, b_k are evaluated by the least square fit method. The procedure reduces to the Fourier transformation, and a_k, b_k are given as

$$a_k = \frac{2}{T}\int_0^T Q(t)\cos(k\omega t)dt \tag{3.30}$$

$$b_k = \frac{2}{T}\int_0^T Q(t)\sin(k\omega t)dt \tag{3.31}$$

The amplitude c_k and the phase angle δ_k are defined as

$$c_k = \sqrt{a_k^2 + b_k^2} \tag{3.32}$$

$$\tan(\delta_k) = a_k / b_k \tag{3.33}$$

The time series of the flow properties are reduced to two scalar parameters, and it becomes possible to discuss unsteady behavior of the flowfield from the still contour plots of c_k and δ_k.

3.2.2 Frequency Filter

The fluctuation of realistic flowfield is usually composed of several frequency components. Each component corresponds to its own phenomenon, and in many cases, if not always, it help our understanding the mechanism of the flowfield to distinguish and discuss each component one by one. However, it is difficult to distinguish each component when the amplitude of different components are in the same order.

Figure 3.1 shows an example of oscillation at two different points. The oscillations shown in 3.1 are composed of three components with different frequencies. Each component is shown in Figs. 3.2(a)$\sim$3.2(c). It is not difficult to understand the relationship (i.e. amplitude ratio and phase difference) between two oscillations for each component one by one. But once three components are superimposed into one (Fig. 3.1), it is almost impossible to distinguish each component from the time history. Frequency filters are often used to separate fluctuations with different frequencies in the post-processing of experiments. As a straightforward extension of this technique, time series of the physical properties at all nodes are processed by the frequency filters, and the secondary processed data instead of the raw data is visualized.

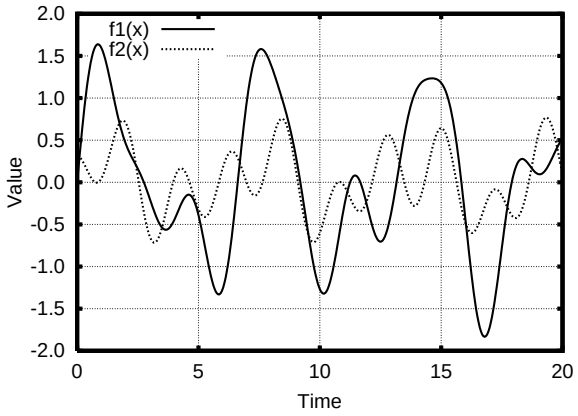

Figure 3.1: Time histories of the physical property

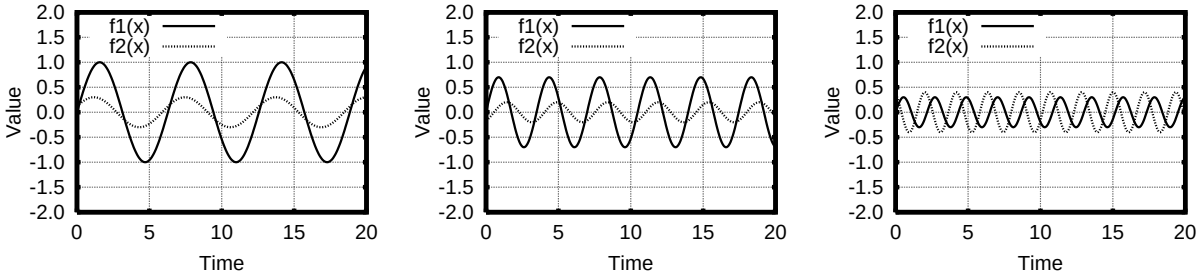

(a) $f = 6.28$ (b) $f = 11.31$ (c) $f = 18.22$

Figure 3.2: Time histories of the each component

Filtering procedure

The post-processing procedure of the unsteady simulation result using a frequency filter is as follows:

(1) extract time history of a flow variable at a node that represents the flowfield

(2) decompose the time history into modes using Fourier analysis

(3) select the mode to visualize

(4) process the time history of the flow variables at all nodes by the frequency filter to eliminate surplus modes

(5) visualize the filtered flow variables

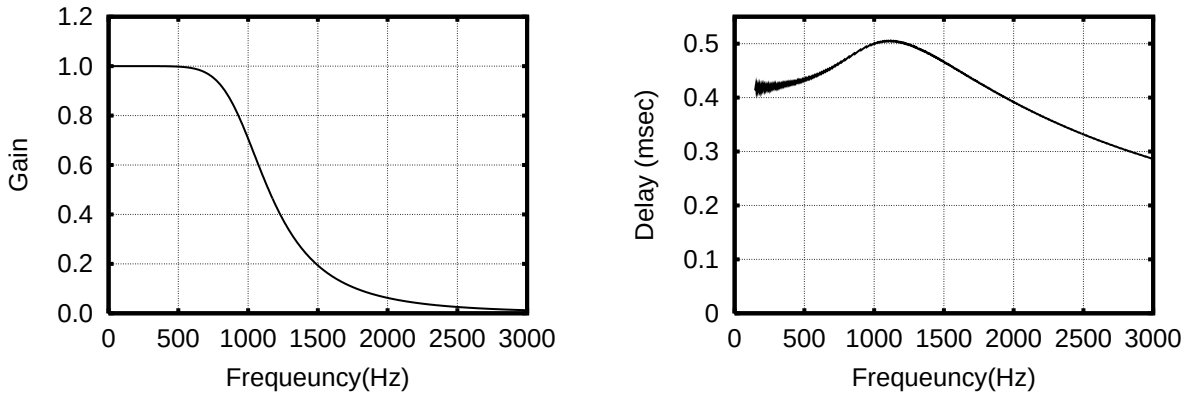

(a) gain (b) delay

Figure 3.3: Characteristics of the Butterworth filter

(6) create animation

the steps (5) and (6) are the same procedure as those used in the ordinary post-processing of the unsteady simulations, However, the complicated fluctuation is already divided into components by the filtering, and the mechanism of each components can be discussed separately. It will be easier to understand the flowfield with this method.

Digital filter

n-th order digital filter stores n data sets on the main memory as a temporary variable. The numerical simulation using millions of nodes outputs tens to hundreds MB data file. On the other hand, the main memory size of the modern workstation is hundreds MB to several GB. Therefore, allowable order of the filter is ten at the maximum. It is difficult to achieve sharp cut-off characteristic with 10th order FIR digital filter, and the IIR digital filter[20] is used in the present study

Figure 3.3 show the characteristics of the 4th order Butterworth low-pass filter as an example of the IIR digital filter. The cut-off frequency f_c is 1000Hz The filter cause 0.4 msec of delay at the low frequency region, and therefore the delay has to be compensated when comparing the filtered value with the non-filtered property. The delay also shows

distortion near the cut-off frequency 1kHz. The cut-off frequency has to be carefully selected so that it is kept far away from the dominant frequency of the phenomena. Otherwise, the filtering process distorts the flowfield and may outputs misleading results.

CHAPTER 4

FLOWFIELD AROUND THE CAPSULE IN THE PITCHING OSCILLATION

The flowfield around the oscillating capsule is very complicated, and it is difficult to discuss the mechanism of the dynamic instability in detail without the general understandings of the flowfield. In this chapter, the flowfield around the capsule under the forced pitching oscillation is simulated on a relatively coarse grid, and the behavior of the oscillation of the flowfield is discussed.

4.1 Method of Analysis

4.1.1 Flow Configuration

The simulation in this chapter basically follows Hiraki's experiment. The flowfield around the oscillating D45 model capsule, which was dynamically unstable at transonic speeds in the experiment, is numerically simulated and discussed. Hiraki's experiment was carried out with one-dimensional free oscillation method, but the limit cycle oscillation of the capsule observed in the experiment was almost sinusoidal, and therefore the motion of the capsule is approximated by the forced sinusoidal oscillation in the present simulation.

The numerical conditions are shown in Table 4.1. The period of the oscillation is 149.7 in non-dimensional time unit, and the time step Δt is set to be 1/150,000 of the period. The simulation starts from the steady state solution of zero angle of attack. During the

Table 4.1: Flow conditions

Mach number	1.3
Dia. of the capsule	0.1 m
Re number	2.5×10^6
Frequency	20 Hz
Max. pitch angle	$\pm 20^\circ$
Reduced frequency	0.0323

computation, overall aerodynamic forces are monitored. The history of the forces at the third cycle coincides with that at the second cycle, and the flowfield is considered to have reached to the periodic state in two cycles. Seven oscillation cycles are simulated after the flowfield reached to the periodic state to accumulate the unsteady flowfield data.

The simulations are carried out on 4PE of the Fujitsu VPP500/7 at the ISAS, and it required 40 hour to compute one oscillation cycle.

4.1.2 Grid Systems

The computational grid is shown in Fig. 4.1. The grid consists of $121 \times 64 \times 61$ points. The minimum grid spacing at the wall is 6.0×10^{-5} so that it captures the turbulent boundary layer. The computational domain ranges from -2.0 to 10.0 in the x direction and -10.0 to 10.0 in the y and z directions. The whole grid system oscillates around the center of the gravity of the capsule $(x_{CG}, 0, z_{CG})$ in pitch sinusoidally. The velocity at each node is given by

$$\begin{cases} x_t = (z - z_{CG})\theta_{max}\omega\cos(\omega t) \\ y_t = 0 \\ z_t = -(x - x_{CG})\theta_{max}\omega\cos(\omega t) \end{cases} \tag{4.1}$$

The influence of the body motion is reflected to the simulation through the temporal components of the metrics and the solid wall boundary conditions (Eq. (3.26)). The outer boundary is placed far enough $(10D)$ from the capsule. and the results of the simulation show that all the disturbance are damped out inside the computational domain. Therefore

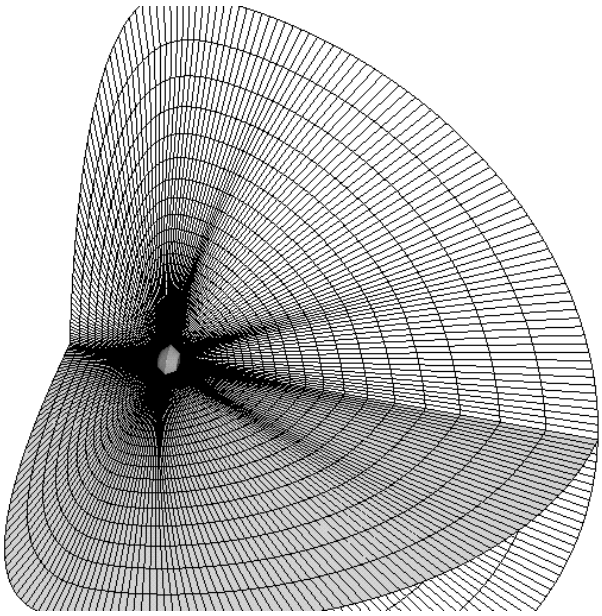

Figure 4.1: Computational Grid ($121 \times 64 \times 61$)

the outer boundary condition that fix all the physical properties to the uniform flow condition is considered to be reasonable for this simulation.

4.1.3 Post Processing

Instantaneous physical properties of the flowfield are saved every 1,000 time steps to the files, and 150 data files (1.3 gigabytes in size) are created each cycle. The physical properties are defined on the moving grid fixed to the capsule, but the grid system fixed to the space is sometimes more convenient for the analysis of the amplitude and the phase. The physical properties are mapped over the equally spaced rectangular grid fixed to the space as shown in Fig. 4.2, and time series of data are obtained at each point. The time series of data are then processed by the Fourier analysis, and the spatial distribution of the amplitude and the phase are obtained.

The flowfield away from the capsule is mainly discussed on the rectangular grid, and the physical properties at the surface of the capsule is discussed on the original body-fitted grid system in this chapter.

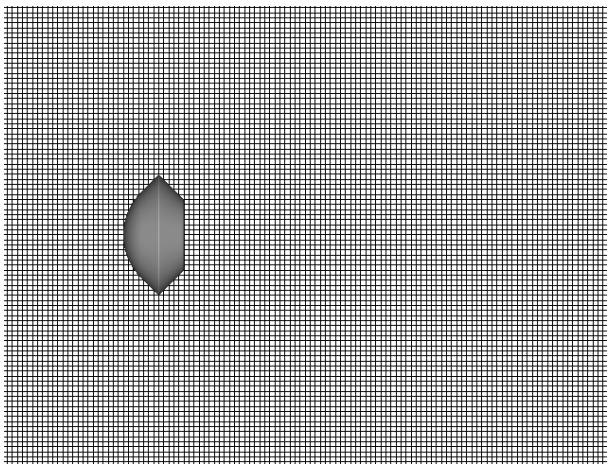

Figure 4.2: Grid used in post processing

4.2 Overview of the Flowfield

Figure 4.3 shows the instantaneous density gradient distribution around the capsule in the forced pitching oscillation. The capsule is at zero angle of attack, and it is in the pitch-up motion at the moment of the Fig. 4.3 The bow shock wave is formed ahead of the capsule. The flow separates at the edge of the capsule and forms shear layer behind the capsule. The shear layer converges as it goes downstream due to the strong expansion at the edge, and the recompression shock wave emanates from the neck point of the wake. The oscillation of the flowfield is shown in Fig. 4.4. [1] The fundamental flow features do not change even when the capsule oscillates, although their locations move with the pitch angle of the capsule; the upper half of the bow shock wave moves backward and lower part moves forward, and the wake downstream moves upward, when the capsule is pitched up. Figure 4.4 also shows that the flowfield oscillates with hysteresis. The wake passes slightly below the centerline when the capsule is pitching up at $\alpha = 0°$, while it passes upper side when the capsule is pitching down at $\alpha = 0°$. The flowfield downstream varies depending on the direction of the pitching motion of the capsule.

The flowfield behind the capsule is essentially unsteady due to the vortex shedding

[1] Animation is available in the attached CD-ROM. See Appendix D

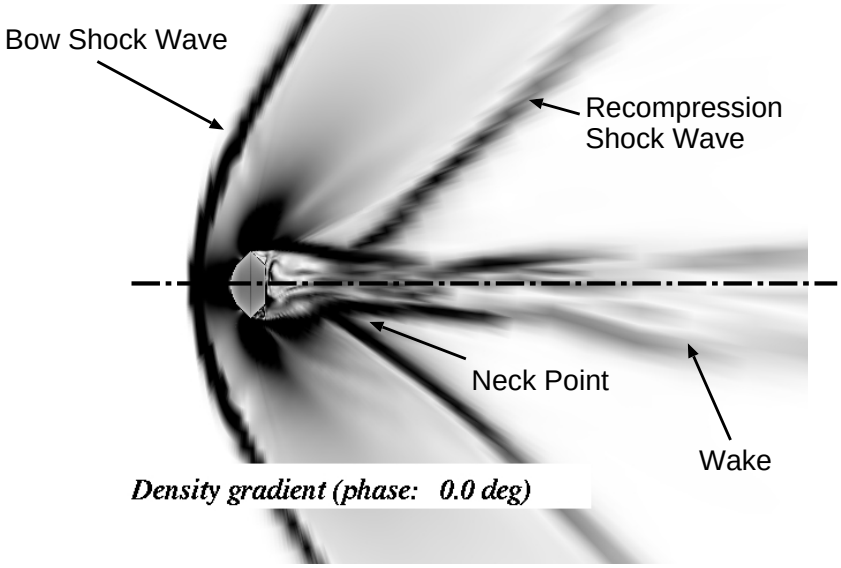

Figure 4.3: Instantaneous density gradient distribution

from the edge of the capsule. The power spectrum density of the base pressure of the capsule in the forced pitching oscillation (20Hz) and that of the capsule fixed at zero angle of attack are compared in Fig.4.5. The base pressure of the capsule fixed at $\alpha = 0°$ oscillates at approximately 770Hz, which corresponds to the Strouhal number $St = 0.256$, due to the vortex shedding and no distinct peak is observed below 400Hz. Figure 4.5 shows that the lowest natural frequency of the flowfield is 770Hz for this flow configuration. When the capsule oscillates in pitch at 20Hz, the peak that corresponds to the vortex shedding shifts higher to 1000Hz, and new peaks appear at 20Hz and 40Hz. These peaks are the harmonic fluctuation induced by the pitching motion of the capsule. Although high frequency fluctuation is noticeable behind the capsule, its frequency is far higher than that of the oscillation of the capsule, and it seems that the high frequency disturbance does not directly contribute to the dynamic instability of the capsule. The pitching oscillation of the capsule induces only the harmonic fluctuations to the flowfield, and therefore we can focus only on the harmonic component of the oscillation of the flowfield in the following discussions.

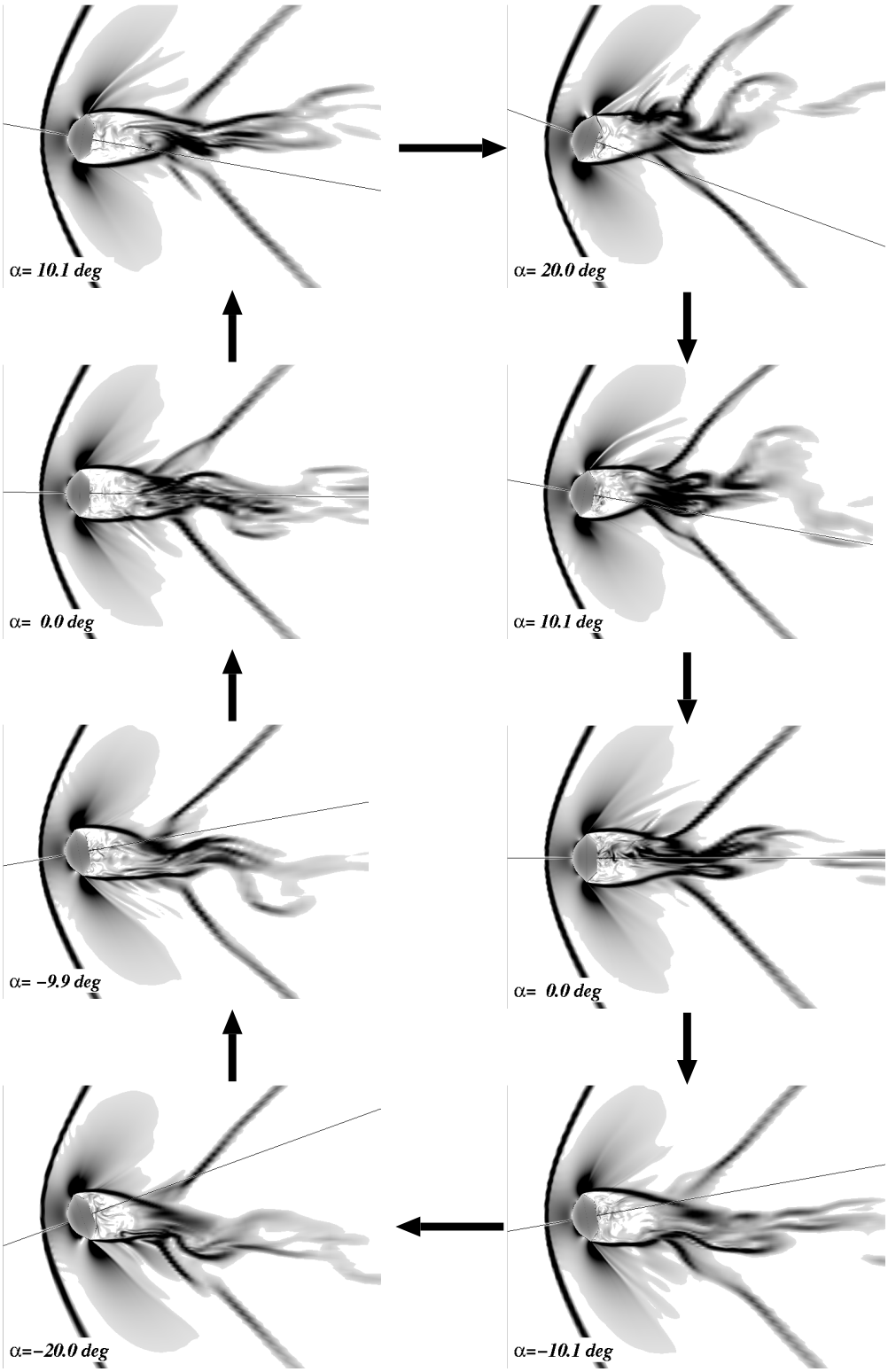

Figure 4.4: Flowfield around the oscillating capsule

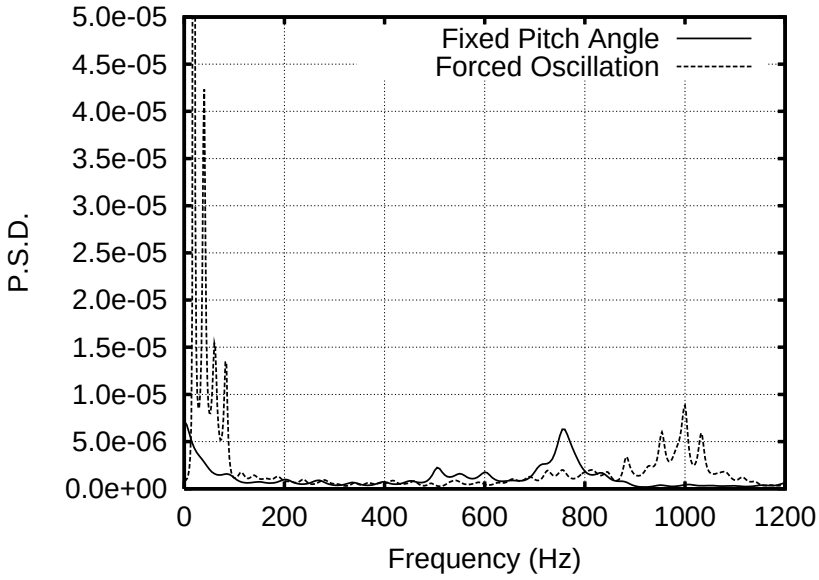

Figure 4.5: Power spectrum density of the base pressure

4.3 Pitching Moment and Surface Pressure

4.3.1 Pitching Moment

The aerodynamic pitching moment around the axis of rotation is plotted against the pitch angle in Fig. 4.6. The gradient of the moment, $\frac{\partial M}{\partial \theta}$ is negative. The aerodynamic moment works to suppress the pitch angle of the capsule, therefore the capsule is statically stable in the pitch. Hysteresis of the moment is also observed in Fig. 4.6. The pitching moment is higher when the angular velocity is positive than when the angular velocity is negative. Consequently, net work-input to the capsule during one oscillation cycle is positive, and the amplitude of the oscillation grows up. The capsule is dynamically unstable under this enforced oscillation although it is statically stable.

4.3.2 Surface Pressure

Time histories of the surface pressure at two locations; one in the front and the other in the base part of the capsule, are plotted with the history of the pitch angle in Fig. 4.8. Both

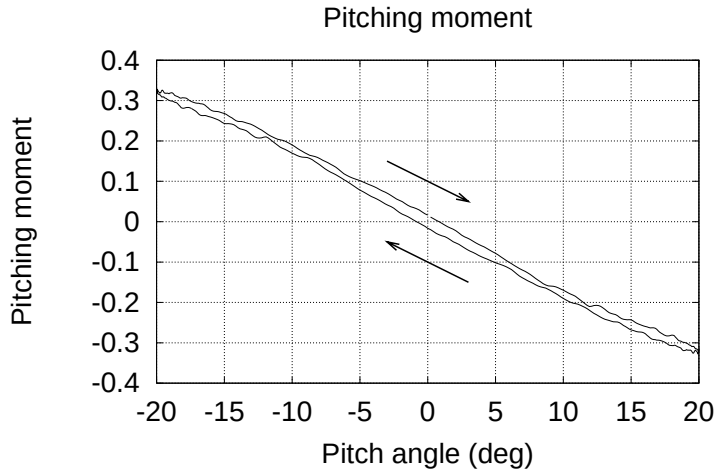

Figure 4.6: Pitching moment works to the capsule

are located in the plane of symmetry of the capsule, and their positions are shown in Fig. 4.7. The cross symbols in Fig. 4.8 denote the instantaneous surface pressure obtained by the numerical simulation, and the dashed lines are the first harmonic component obtained from the Fourier analysis. The history of the base pressure is processed by the LPF with cut-off frequency of 150Hz to eliminate high frequency fluctuations.

The surface pressure at the front point varies synchronously with the pitch angle; the pressure is same at the same pitching angle both in the pitching up and down. Therefore, the front pressure does not contribute to the hysteresis of the pitching moment. On the other hand, the base pressure oscillates with a phase delay against the pitch angle. The base pressure at a certain pitch angle varies depending on the direction of the pitching motion and hence, the pitching moment due to the base pressure shows hysteresis. The pressure at the upper part of the base is higher when the pitch angle is positive, and the higher static pressure at the base rotates the capsule pitching-down. The base pressure works on the capsule to make it statically stable. In general, a system that is statically stable becomes dynamically unstable when the system works with delay, and therefore the phase delay of the base pressure makes the capsule dynamically unstable.

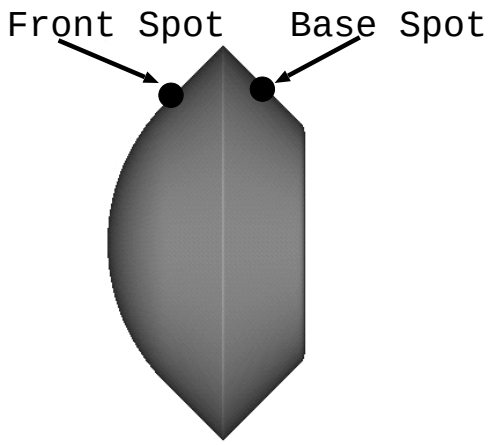

Figure 4.7: Location of pressure port

The dynamic instability of the capsule is caused by the hysteresis of the pitching moment, and it is the phase delay of the backside pressure that produces the hysteresis.

4.4 Fluctuation of the Pressure Field

Time histories of the static pressure at all the nodes are processed by the Fourier analysis, and the spatial distribution of the amplitude and the phase are obtained. Figure 4.9 shows the distribution of the phase angle of the oscillation of the static pressure. Only the region where the phase angle is between $-20°$ and $+20°$ is displayed, and the white region indicates the area where the phase is delayed. The contour plots of the density gradient are plotted in the bottom half for reference. The pressure phase along the dashed lines A and B in Fig. 4.9 are plotted in Figs. 4.10 and 4.11 respectively.

The flowfield can be divided into following three regions:

Region 1: The recirculating region surrounded by the capsule, shear layer and the recompression shock wave

Region 2: Wake region downstream of the recompression shock wave

Region 3: Flowfield outside of the wake

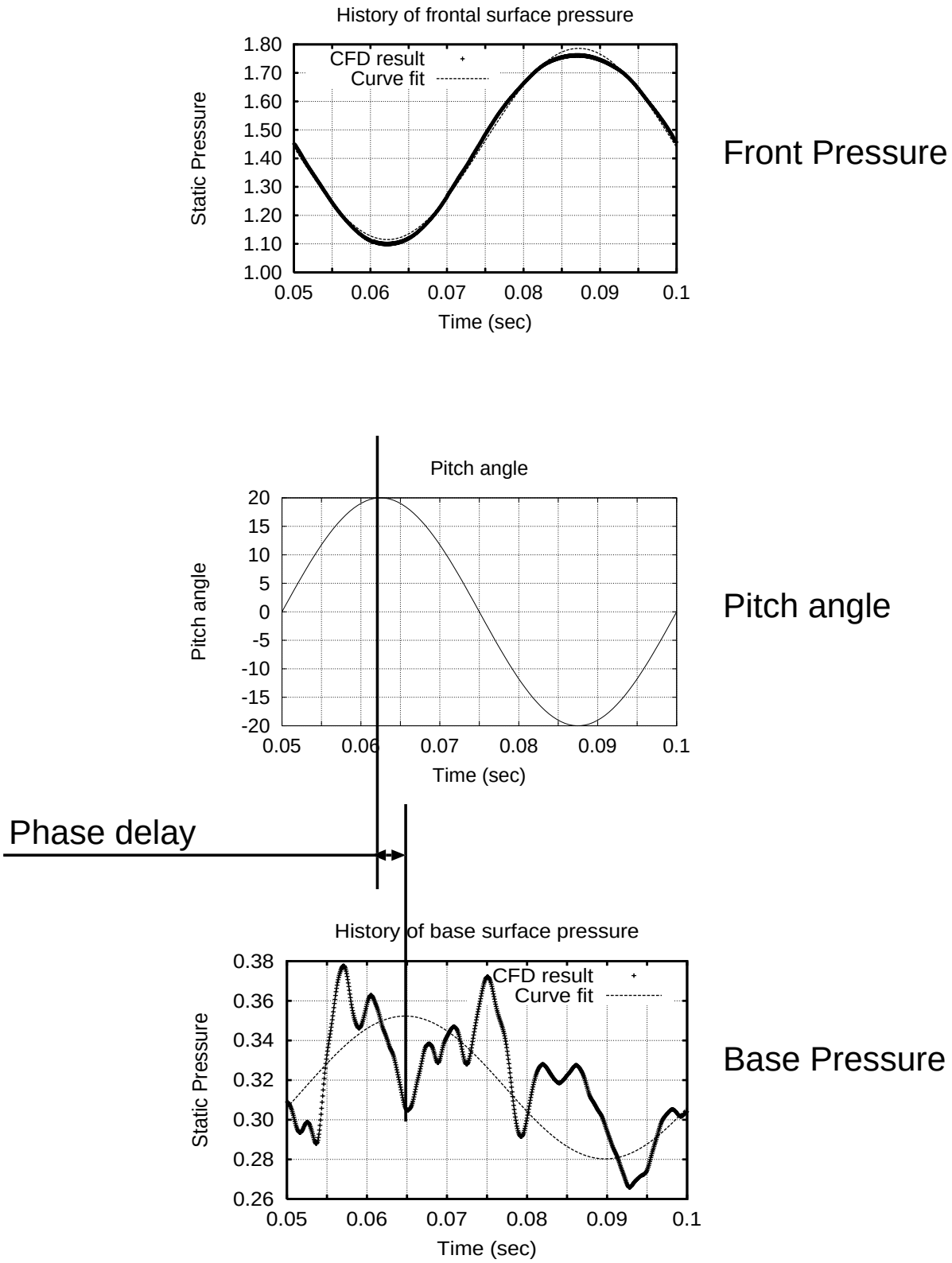

Figure 4.8: History of surface pressure

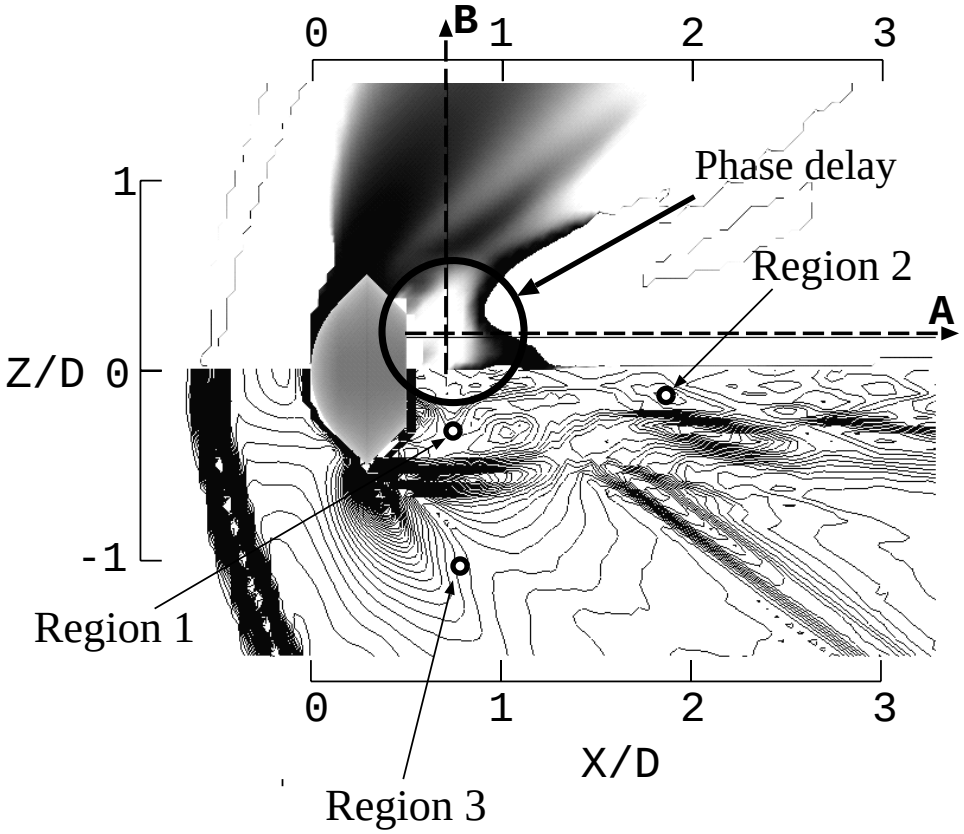

Figure 4.9: Top: Pressure phase distribution, Bottom: Density gradient distribution

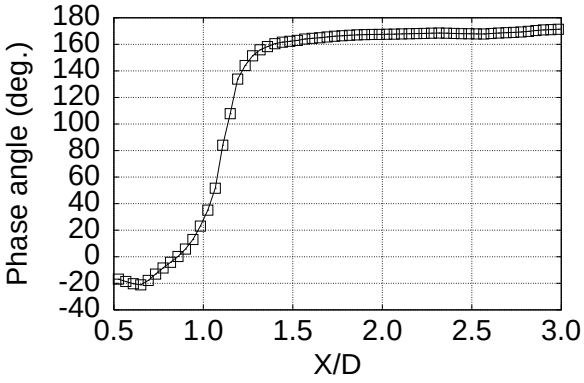

Figure 4.10: Pressure phase along line A

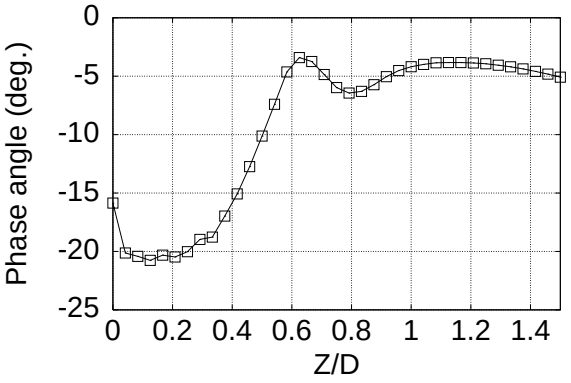

Figure 4.11: Pressure phase along line B

Figures 4.9 to 4.11 show that the pressure phase is delayed only in the Region 1. The flowfield is supersonic at the Region 3, and the pressure at this region is directly influenced by the upstream flowfield which is coupled with the attitude of the capsule. Therefore the phase delay angle at the this region is almost zero. Figure 4.11 shows that the phase angle is nearly constant inside both the Region 1 and Region 3, and it changes rapidly at the shear layer at $Z/D \simeq 0.5$. The gradient of the phase angle at the shear layer is as large as 14 (rad/m). One-dimensional propagation of a disturbance wave is described as

$$f(x,t) = f_0 e^{i\omega\left(t-\frac{x}{C}\right)}$$

where i is the imaginary unit and C is the speed of the wave. The phase angle ϕ is given by

$$\phi(x,t) = \omega\left(t - \frac{x}{C}\right)$$

therefore the spatial gradient of the phase angle caused by the propagation is

$$\frac{\partial\phi}{\partial x} = \frac{\omega}{C} = \frac{2\pi f}{C}$$

The flowfield considered in this study is transonic, and the value of the characteristic speeds u, c and $u \pm c$ are all hundreds m/s. If the pressure fluctuations at the Region 1 and the Region 3 are directly correlated each other, the gradient of the phase angle should be $\frac{2\pi f}{c} \simeq 0.4$(rad/m) at the interface of two regions, therefore the gradient of 14(rad/m) along the line B is unreasonably large for the transonic flowfield. It indicates that the fluctuation inside the Region 1 is not directly influenced by the fluctuation at the Region 3. The pressure at the Region 2 oscillates with the phase angle approximately 160°, which is 20° delayed against 180°. The pressure at the Region 2 decreases when the capsule pitches up, but the its oscillation is slightly delayed from the pitch angle, and the delay time is same as that at the Region 1. Since the pressures at two regions

oscillate with the same delay time, the pressure right behind the capsule is considered to be coupled with the flowfield downstream of the neck point.

4.5 Oscillation of the Shock Wave and the Wake

The oscillation of flow variables other than the pressure is discussed in this section.

The amplitude and the phase of the fluctuation of the radial position of the wake along the section B-B in Fig. 4.12 are shown in Table 4.2. The wake at the section B-B represents the interface between the Region 1 and Region 3. Since the position of the capsule's edge moves when the capsule oscillates, the deviation of the edge position is subtracted from that of the wake position at the analysis of the phase and the amplitude. The amplitude of the oscillation is less than 2% of the diameter of the capsule, and it does not seem that the oscillation of the wake near the capsule directly influences the pressure phase behind the capsule.

Secondly, the axial location of the recompression shock wave along the section A-A in Fig. 4.12 is plotted against time in Fig. 4.13. The recompression shock wave oscillates twice during one cycle of the oscillation of the capsule (0.05 sec). The recompression shock wave takes its most backward position 2.2 msec after the capsule passes the neutral (pitch angle $\theta = 0$) position. Thus, the motion of the recompression shock wave is 2.2 msec delayed from the capsule. The delay time of the recompression shock wave coincides with that of the oscillation of the static pressure at Region 1 and Region 2. Since the recompression shock wave emanates from the neck point, the motion of the shock wave represent the oscillation of the flowfield near the neck point.

The pressure inside the Region 1 and Region 2, and the flowfield around the neck point, which is the interface between two regions, all oscillate with the same delay time. Again, the pressure behind the capsule is considered to be coupled with the flowfield around the neck point.

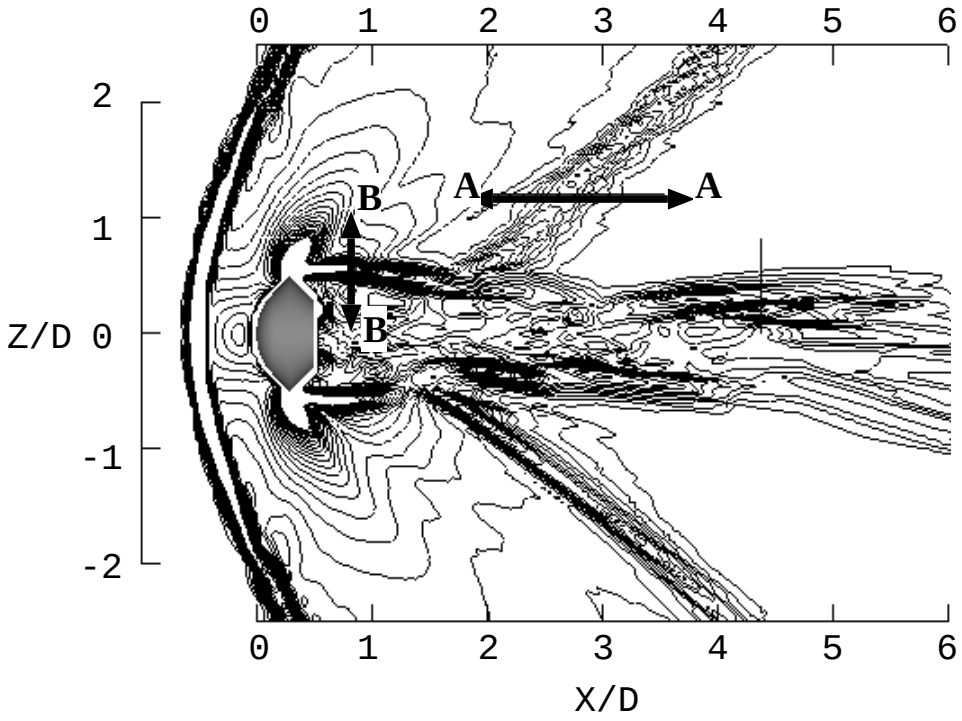

Figure 4.12: Definition of the sections

Table 4.2: Oscillation of the wake near the capsule

	Amplitude	Phase
Section B-B	0.016	-98.40 deg

4.6 Summary

Flowfield around a capsule oscillating at transonic speed is numerically simulated. It becomes clear that the dynamic instability of the capsule is caused by the phase delay of the base pressure.

The pressure right behind the capsule, the pressure downstream of the recompression shock wave and the recompression shock wave that emanates from the neck point all oscillate with the same delay time. It indicates that the base pressure is coupled with the flowfield near the neck point Therefore, delay in the transition of the flowfield near the neck point is the cause of the delay in the oscillation of the base pressure.

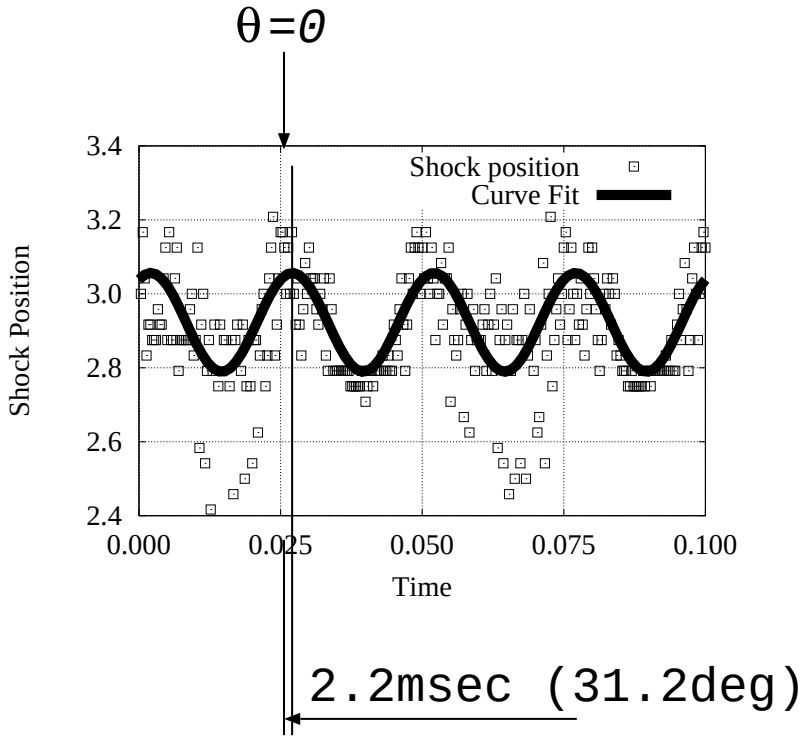

Figure 4.13: Shock location along line A-A

CHAPTER 5

EVALUATION OF THE DYNAMIC CHARACTERISTICS BY A SIMPLE CONSTANT-DELAY MODEL

The study in chapter 4 revealed that the dynamic instability of the capsule is caused by the delay of the aerodynamic pitching moment. However, the flowfield behind the capsule is scattered by the high frequency disturbances, and it is still difficult to discuss the mechanism of the dynamic instability.

Fortunately, the reduced frequency of the oscillation is as low as $O(0.01)$, and the motion of the capsule is very slow compared to the characteristic time of the flowfield. The fundamental flow structures such as the shock wave and the wake are not changed by the pitching motion of the capsule, and the influence of the motion upon the flowfield seems to be small. Considering these characteristics, the flowfield around the oscillating capsule may be reasonably modeled by the flowfield around the capsule which changes its pitch angle in a quasi-steady manner. If this is the case, it becomes possible to discuss the mechanism of the dynamic instability by the simulation of the flowfield around the capsule at fixed pitch angle, with consideration of constant time delay of the backside pressure. There is no need to process gigabytes of data, and it will be easier to discuss the mechanism of the flowfield with this approach.

In this chapter, the flowfields around the capsule fixed at certain pitch angle and

Table 5.1: Flow conditions

	forced oscillation	fixed pitch angle
Mach number	1.3	
Dia. of the capsule	0.1 m	
Re number	2.5×10^6	
Pitch angle	forced sinusoidal oscillation Frequency : 20 Hz Max. pitch angle : $\pm 20°$ Reduced frequency : 0.0323	0°, 2.5°, 5°, 7.5°, 10°, 15°, 20°

that around the oscillating capsule are numerically simulated, and the difference in the aerodynamic pitching moment is discussed.

5.1 Method of Analysis

5.1.1 Flow Configuration

The geometry of the capsule and the uniform flow conditions are same as those of the simulation in chapter 4.

The flowfield is highly unsteady even when the pitch angle is fixed, and the time step is defined small enough to resolve the unsteady fluctuation of the flowfield. The time step Δt for the simulation of the oscillating capsule is 1/150,000 of one oscillation cycle again, and the time step for the simulation of fixed pitch angle is set to be 0.001 in non-dimensional time unit. Δt is approximately 3.4×10^{-7} second in physical time unit for both cases. The numerical results showed that the highest dominant frequency of the flowfield is approximately 1 kHz which corresponds to the Strouhal number ($St = fD/u$) of 0.27, and therefore $\Delta t = 3.4 \times 10^{-7}$ second is small enough to resolve the unsteady fluctuation of the flowfield.

The simulations are carried out on the Fujitsu VPP800/12 at the ISAS. It required 20 hour on 4PE of VPP800/12 to compute one forced oscillation cycle. The simulations for the fixed pitch angle are carried out on single PE, and each case required approximately

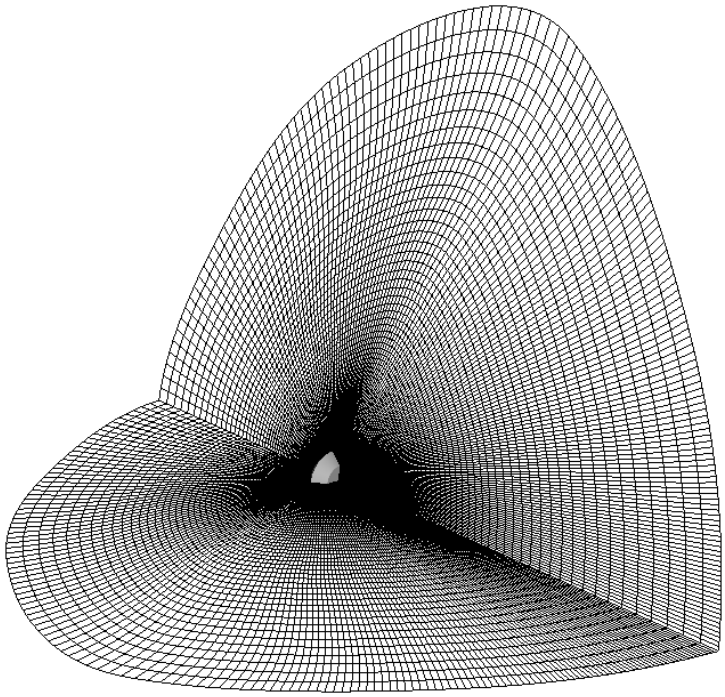

Figure 5.1: Computational Grid ($151 \times 64 \times 121$)

30 hour.

5.1.2 Grid Systems

The grid used in this study is shown in Fig. 5.1. The grid consists of $151 \times 64 \times 121$ points with O-O topology, and the grid are clustered at the base region to resolve the flowfield behind the capsule. The minimum grid spacing at the wall is 2.0×10^{-5}, and the computational domain ranges from -4.0 to 10.0 in the x direction and -10.0 to 10.0 in the y and z directions. The Courant number is smaller than 0.3 with $\Delta t = 1/1000$, except for the region near the wall ($\delta < 0.04$).

5.1.3 Post Processing

Figure 5.2 shows the time history of the static pressure at a point at the base of the D45 model fixed at $\alpha = 10°$. High frequency fluctuation is observed although the pitch

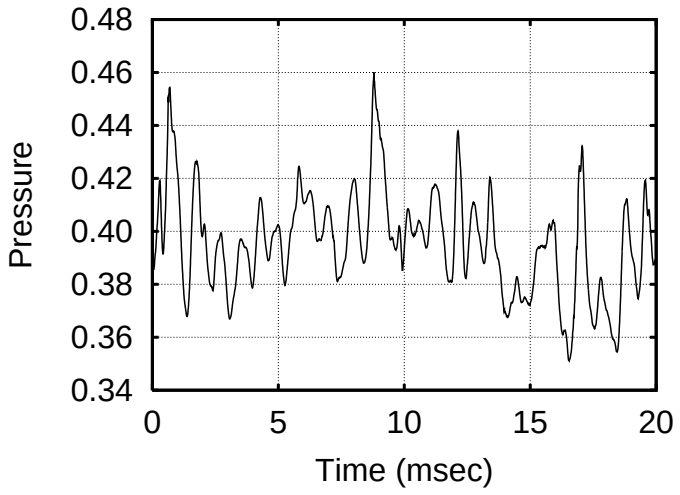

Figure 5.2: Time history of the base pressure of the D45 model fixed at $\alpha = 10°$

angle of the capsule is fixed. The amplitude of the oscillation reaches 10% of the average pressure, and its frequency is approximately 1kHz. The high frequency fluctuation is also observed in the simulation result of the forced pitching oscillation (Fig. 4.5). These disturbances correspond to the shedding of small vortices from the edge of the capsule. Since the time scale of the vortex shedding (1KHz) is totally different from that of the oscillation of the capsule (20Hz), the slow oscillation of the capsule does not seem to influence the high frequency shedding of the small vortices. The behavior of the small vortices are considered to be the same both for the capsule fixed at certain pitch angles and the capsule oscillating in pitch. The influence of the slow pitching oscillation of the capsule on the flow structure is the primary concern in this chapter, and therefore the influence of the high frequency component should be excluded for the low frequency component to be clearly observed.

For the simulation of the fixed pitch angle cases, the physical properties are summed up during 20,000 steps (approximately 7msec in the real time unit) after the flowfield have reached to the stationary state, and the time averaged properties are used for the discussion. The average time of 7msec is considered to be long enough for the disturbance

at nearly 1kHz oscillation to be excluded.

The physical properties obtained from the forced-oscillation simulation are processed by the Low Pass Filter (LPF) with cut-off frequency of 150Hz for the high frequency fluctuation to be eliminated. Since the LPF cause delay to the output data, the filtered history of the physical properties can not be compared with the raw history of the pitch angle directly. The history of the pitch angle is also processed by the same LPF to compensate the delay caused by the LPF. The dominant frequency of the flowfield is 20Hz, which is low enough compared with the cut-off frequency, and the LPF does not distort the fundamental behavior of the flowfield.

5.2 Simple Constant-Delay Model

Overall aerodynamic pitching moment due to the static surface pressure that works on the capsule is given as $M = \oint p\vec{n} \times \vec{r} \cdot ds$. The flowfields in front and back of the capsule are considerably different each other, and therefore we separate the contribution from the front pressure and that from the base pressure as follows:

$$M = M_f + M_b \tag{5.1}$$

$$\begin{cases} M_f(\alpha) &= \oint_{\text{front area}} p\vec{n} \times \vec{r} \cdot ds \\ M_b(\alpha) &= \oint_{\text{base area}} p\vec{n} \times \vec{r} \cdot ds \end{cases} \tag{5.2}$$

If the surface pressure of the capsule oscillates with the delay time δ against the pitch angle ("constant-delay model") when the capsule oscillates in pitch with $\alpha = \alpha_{\text{MAX}} \sin(\omega t)$, the aerodynamic pitching moment works on the capsule during the oscillation will be described as

$$M_{f\,\text{delay}}(t) = M_{f\,\text{fixed}}\left(\alpha_{\text{MAX}} \sin(\omega(t - \delta_f))\right) \tag{5.3}$$

$$M_{b\text{delay}}(t) = M_{b\text{fixed}}\left(\alpha_{\text{MAX}}\sin(\omega(t-\delta_b))\right) \tag{5.4}$$

where the subscript "fixed" denotes the moment works on the capsule at fixed pitch angle, and "delay" denotes the constant-delay model. The result of the forced-oscillation simulation in chapter 4 showed that $\delta_f \simeq 0$ and $\omega\delta_b \ll 1$, then

$$\begin{aligned} M_{(t)} &= M_{f\,\text{delay}}(t) + M_{b\text{delay}}(t) \\ &= \left(M_{f\,\text{fixed}(\alpha)} + M_{b\text{fixed}(\alpha)}\right) - \delta_b \left.\frac{\partial M_{b\text{fixed}}}{\partial\alpha}\right|_{\alpha} \dot{\alpha} + O(\alpha^2) \end{aligned} \tag{5.5}$$

The M_b shows strong non-linearity at small angles of attack, as shown in the next section, and the higher order terms in Eq.(5.5) is not negligible. However, Eq.(5.5) describes general characteristics of the aerodynamic pitching moment.

The aerodynamic pitching moment works on the object placed in a uniform flow is expressed using aerodynamic coefficients as follows

$$M = \frac{1}{2}\rho_\infty u_\infty^2 SD \cdot \left(C_m + \left(C_{mq} + C_{m\dot{\alpha}}\right)\frac{D}{u_\infty}\dot{\theta}\right) \tag{5.6}$$

Note that $\theta = \alpha$ since the object is placed in the uniform flow.

Comparing Eq.(5.5) and (5.6), it gives [1]

$$C_m \propto M_{f\,\text{fixed}}(\alpha) + M_{b\text{fixed}}(\alpha) \tag{5.7}$$

$$C_{mq} + C_{m\dot{\alpha}} \propto -\delta_b \left.\frac{\partial M_{b\text{fixed}}}{\partial\alpha}\right|_{\alpha} \tag{5.8}$$

Since M_f is much larger than M_b, Eqs. (5.7) and (5.8) tell that the static aerodynamic characteristics of the capsule depends mainly on M_f, while the dynamic characteristic is mainly determined by the gradient of M_b. The gradient of M_b is evaluated from the simulations of the flowfield around the capsule at fixed pitch angles, and therefore the

[1] These expressions are compared with the Hiraki's expression. See Appendix C

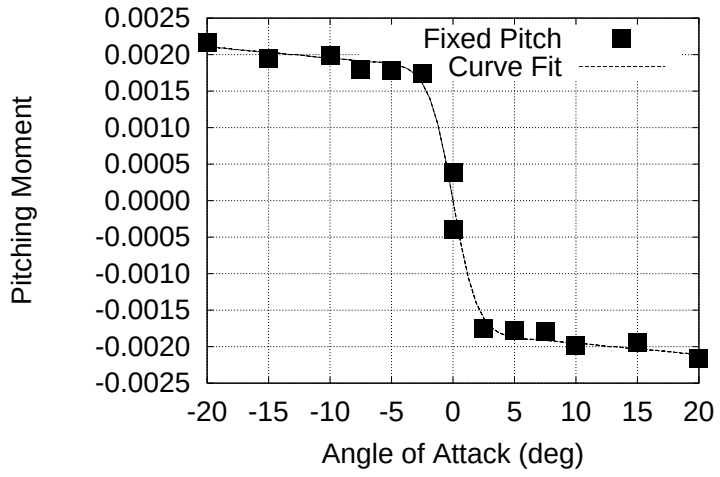

Figure 5.3: Base pitching moment of the D45 Model (Fixed pitch angle)

dynamic characteristic of the capsule can be evaluated without the simulation of the forced oscillation, provided that the base aerodynamic pitching moment M_b during the forced oscillation can be approximated by the "constant-delay model" .

5.3 Comparison with the Results of the Forced Oscillation Simulation

The square symbols in Fig. 5.3 show the base pitching moment M_b obtained for the D45 Model capsule fixed at each angle of attack. The pitching moment is almost constant at $M_b \simeq \pm 0.02$ for $|\alpha| \gg 0$, and abruptly reverses its sign at $\alpha = 0$. M_b is approximated by the following equations

$$M_{b\text{fixed}}(\alpha) = \begin{cases} a_M \tanh(b_M \alpha) & |\alpha| < \alpha_{M0} \\ c_M(\alpha - \alpha_{M0}) + a_M \tanh(b_M \alpha_{M0}) & \alpha > \alpha_{M0} \\ c_M(\alpha + \alpha_{M0}) - a_M \tanh(b_M \alpha_{M0}) & \alpha < -\alpha_{M0} \end{cases} \tag{5.9}$$

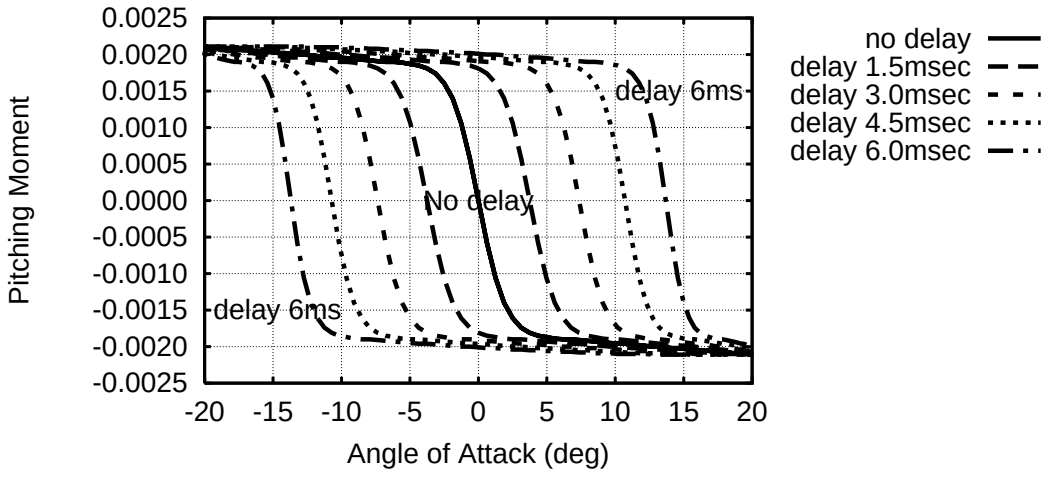

Figure 5.4: Base pitching moment of the D45 Model (constant-delay model)

$$c_M = a_M b_M (1 - \tanh^2(b_M \alpha_{M0}))$$

$$a_M = -0.0019, \quad b_M = 0.5, \quad \alpha_{M0} = 5.5$$

Substituting Eq.(5.9) into Eq.(5.4) and plotting for the several δ_b, it gives Fig. 5.4. Each curves in the Fig. 5.4 shows the history of the M_{bdelay} evaluated by the "constant-delay model" for the delay time 1.5, 3.0, 4.5 and 6.0 msec, respectively. If the fundamental flow structure behind the capsule is not disturbed by the pitching motion of the capsule, the base pitching moment for the capsule in the forced oscillation may be modeled by the "constant-delay model", and the actual history of M_b will become similar to one of the curves in Fig. 5.4. The solid curve in Fig. 5.5 shows the actual history of the base pitching moment M_b when the D45 Model capsule is in the forced pitching oscillation. The history of M_{bdelay} evaluated from the "constant delay model" is also plotted as symbols in the figure. The magnitude of M_b is almost constant at ± 0.002, and M_b reverses its sign at certain pitch angle. The history of M_b is close to the plots of the "simple constant-delay model" for the delay time roughly $\delta = 3.0$msec.

The base pitching moment M_b during the forced oscillation is reasonably approximated by the simple "constant-delay model". The characteristic of the base pressure

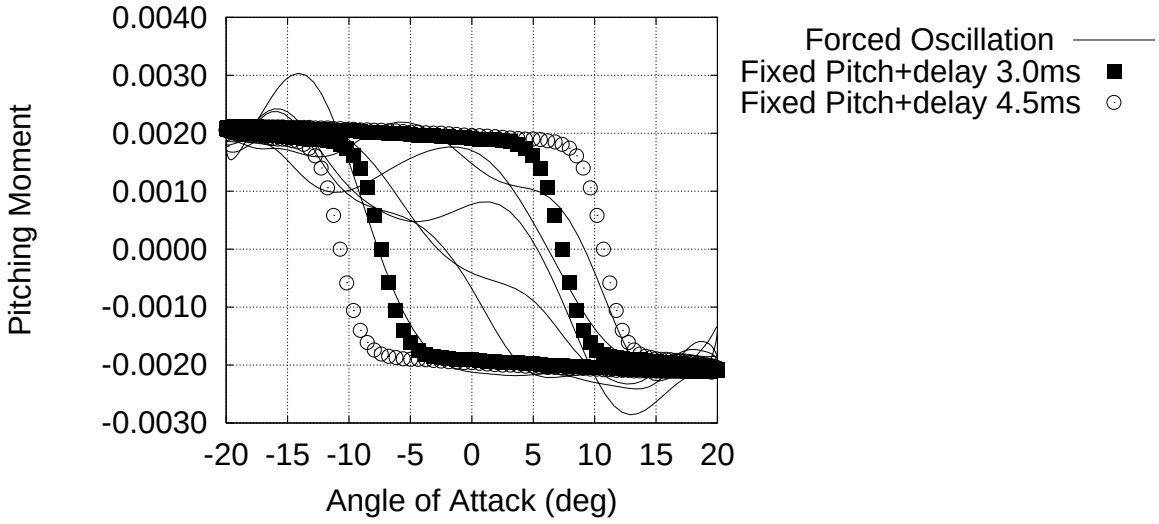

Figure 5.5: Base pitching moment of the D45 Model (Forced oscillation)

distribution reflects the behavior of the flowfield behind the capsule, and therefore it indicates that the flowfield behind the oscillating capsule can also be expressed by the "constant-delay model". That is, the mechanism of the flowfield that determine the base pressure distribution of the oscillating capsule is essentially the same as that for the capsule at fixed pitch angle with the delay time in mind. Therefore, it is possible to discuss the correlation between the flow structure and the dynamic stability of the capsule from the simulation of the flowfield around the capsule at fixed pitch angle.

5.4 Consistency with the Experiment

Figure 5.5 also shows that the hysteresis in the base pitching moment appears at $|\alpha| < 10°$, and the capsule is dynamically unstable only in this region. Hiraki[1] reported from his experiment that the D45 Model capsule is dynamically unstable at small angle of attack, and the constant-delay model is consistent with his experiment.

The base pitching moment of the D30 Model capsule is plotted with the base pitching moment of the D45 Model capsule in Fig. 5.6. The base pitching moment of the D30

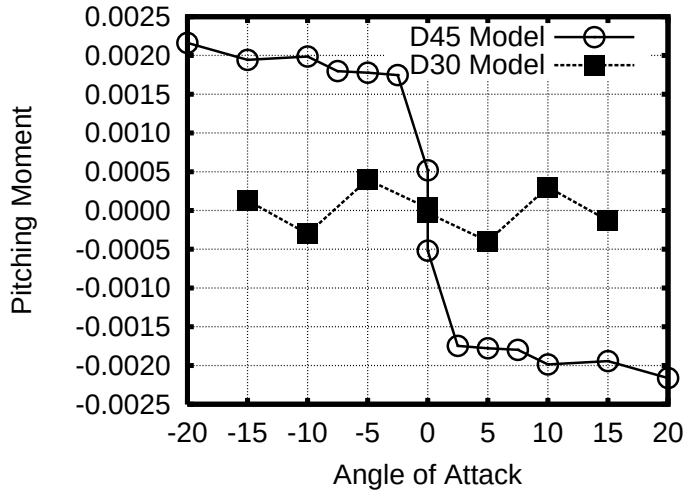

Figure 5.6: Base pitching moment of the D45 & D30 Models (Fixed pitch angle)

Model is almost constant at $M_b \simeq 0$. The pitch damping coefficient $C_{mq} + C_{m\dot{\alpha}}$ is proportional to $\frac{\partial M_b}{\partial \alpha}$ (Eq. 5.8), therefore the D30 Model capsule is predicted to be dynamically neutral or stable from the constant-delay model, and in fact, the D30 Model capsule was dynamically stable in the Hiraki's experiment.

These two results show that this simple constant-delay model are consistent with the characteristic features observed in the past experiments

5.5 Summary

The aerodynamic pitching moment works on the capsule at fixed pitch angle and that works on the capsule in the forced pitching oscillation are compared. The magnitude of the base pitching moment for the capsule at fixed pitch angles are almost constant at $|\alpha| \gg 0$ and reverse its sign abruptly at $\alpha = 0$. The base pitching moment for the capsule in the oscillation also shows similar features except for the small delay, and the history of the base pitching moment is reasonably expressed by the "simple constant-delay model". It indicates that fundamental structure of the flowfield that governs the base pressure distribution is not changed by the pitching motion of the capsule, and

therefore the mechanism of the dynamic stability of the capsule can be discussed by the simulation of the flowfield around the capsule at fixed pitch angle. Considering that the surface pressure is delayed only in the base region, the dynamic stability of the capsule depends mainly on the gradient of the static base pitching moment, $\frac{\partial M_b}{\partial \alpha}$.

CHAPTER 6

FLOWFIELD ANALYSIS FOR THE CAPSULE AT FIXED PITCH ANGLE

The simulation of the flowfield around the capsule under the forced pitching oscillation in chapter 4 showed that the dynamic instability of the capsule is caused by the delay of the base pressure, and the base pressure is governed by large scale flow structure behind the capsule. The flowfield around the oscillating capsule is compared with the flowfield around the capsule at fixed pitch angle in chapter 5. It becomes clear that the flow structure behind the oscillating capsule is essentially same as that behind the capsule at fixed pitch angle, except for the slight delay against the pitch angle.

In this chapter, the flowfield around the capsule at fixed pitch angle is intensively analyzed and the correlation between the flowfield and the base pressure distribution is discussed.

6.1 Flow Configuration

The flowfields around the D45 model capsule and the D30 model capsule are compared in this chapter. The D45 model capsule was dynamically unstable, while the D30 model capsule was dynamically stable in the Hiraki's experiment. Therefore, the difference in the dynamic stability of the two capsules is considered to be related to the difference in the flowfields around two models.

The numerical conditions and the grids are same as those used in chapter 5.

6.2 Base Pressure Distributions

Following the discussion about the characteristic of the pitching moment caused by the base pressure in chapter 5, the characteristic of the base pressure distribution itself is studied.

6.2.1 Time-Averaged Distribution

The time-averaged base pressure distributions along the centerline (line A-A in Fig. 6.1) are plotted against z-coordinate for each pitch angle in Fig. 6.2. The base pressure of the D45 model (Fig. 6.2(a)) uniformly decreases at the region $z < 0.3$ (lower side) as the angle of attack increases. The pressure at $z > 0.3$ also decreases, but for the less amount. The pressure level at $z > 0.3$ is almost the same as that at $z < 0.3$ for the small angle of attacks, but it is higher for the large angle of attacks. The pressure difference between $z < 0.3$ and $z > 0.3$ increases as the angle of attack increases. The high pressure region at the leeward side ($z > 0.3$, upper side of the base) for the positive pitch angle produces pitch-down moment. On the other hand, the base pressure of the D30 model is almost uniform even when the pitch angle is positive (Fig. 6.2(b)), and the base pressure does not produce any pitching moment.

These characteristics are consistent with the characteristics of the base pitching moment M_b shown in Fig. 5.6. Considering that the dynamic stability of the capsule is governed by the gradient of M_b, the flow structure that causes the difference in the time-averaged base pressure distribution is also the cause of the dynamic instability of the capsule.

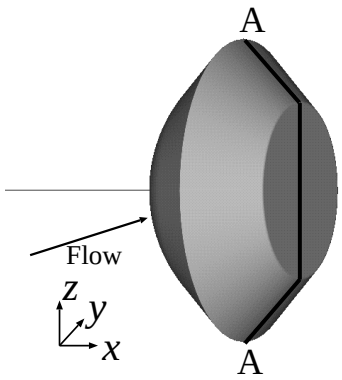

Figure 6.1: Coordinate system

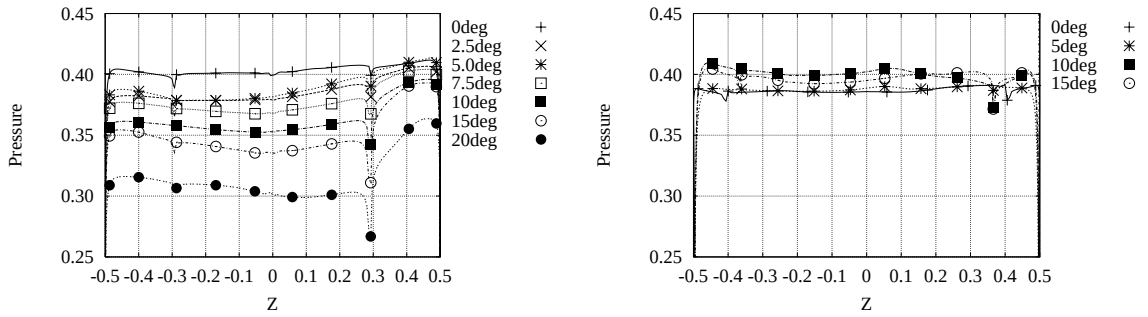

(a) D45 model (b) D30 model

Figure 6.2: Time averaged base pressure

6.2.2 Time History of the Base Pressure

The time-averaged pressure distribution behind the capsule varies linearly with the angle of attack, and the base pitching moment is almost constant for $0° < \alpha \leq 20°$. The fundamental feature of the flowfield behind the capsule is considered to be the same for $0° < \alpha \leq 20°$, and therefore the characteristics of the flowfield is discussed mainly for $\alpha = 10°$ as a representative case.

Time histories of the base pressure at 4 points in the base (shown in Fig. 6.3) of two capsules at $\alpha = 10°$ are shown in Figs. 6.4(a) and 6.4(b). The time-averaged base pressure for the D45 model at $\alpha = 10°$ is approximately 0.36 (Fig. 6.2(a)), and instantaneous base pressure at 3 points, "Right","Bottom" and "Left" fluctuate within

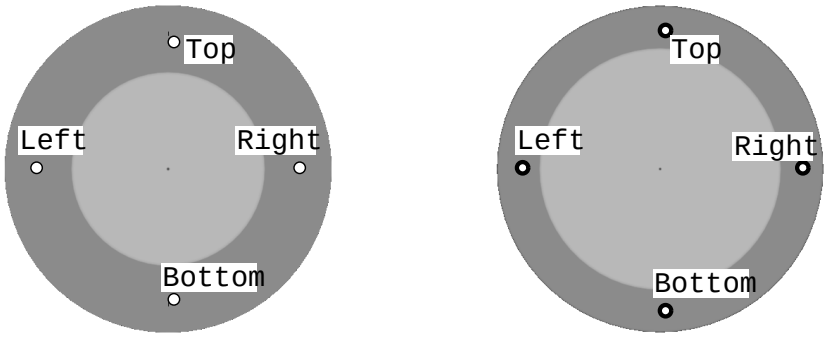

(a) D45 model (b) D30 model

Figure 6.3: Location of the pressure ports (After looking forward)

the range of 0.37 ± 0.01. The pressures at the "Top" also fluctuates around 0.38 with small amplitude for the most part, but it occasionally rises up to approximately 0.45. The pressure at all the 4 ports are almost uniform except for the short pressure peaks. Since the base pressure distribution for the D45 model is described as a superposition of the constant value and the short pressure peaks, the time-averaged pressure distribution depends on the behavior of the pressure peaks. The time-averaged pressure at the leeward (upper) side of the D45 model becomes higher because the pressure peaks appear only in this region.

The base pressure for the D30 model (6.4(b)) is also expressed as the superposition of the constant value and the short pressure peaks, but the peaks appear not only at the "Top" but appear randomly at all the pressure ports. The pressure peaks also exist for the D30 model, but as they appear randomly all over the base, the time-averaged base pressure of the D30 model becomes uniform.

The difference in the characteristics of the time-averaged base pressure reflects the difference in the unsteady behavior of the pressure peaks. Therefore the flow mechanism that cause the pressure peak is considered to be responsible for the dynamic instability of the capsule.

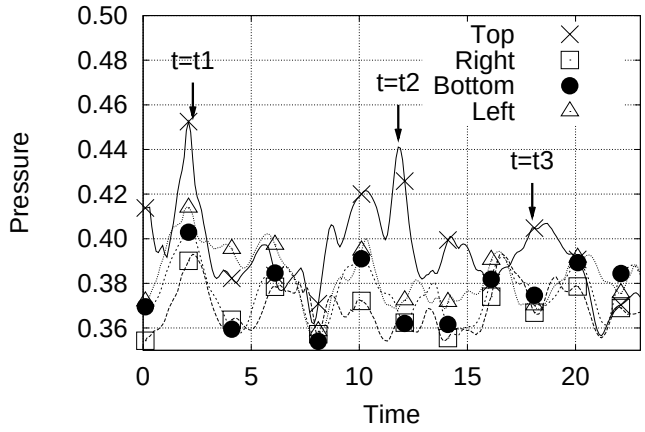

(a) D45 model

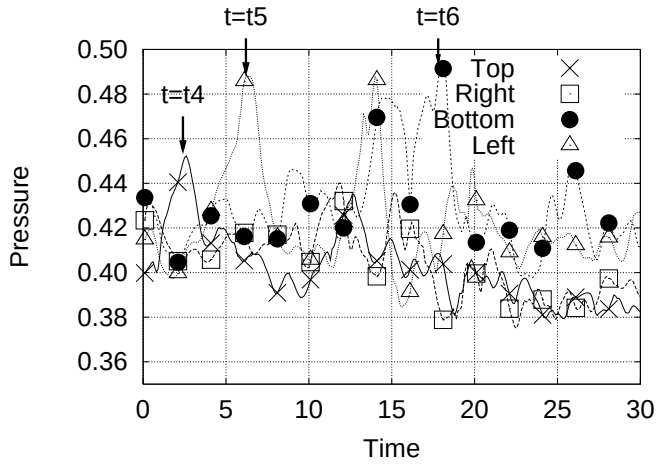

(b) D30 model

Figure 6.4: Time history of the base pressure

6.3 Correlation between the Base Pressure and the Velocity Field

Figure 6.5 shows the time averaged velocity vectors in the plane of symmetry of the D45 model at $\alpha = 10°$. A reverse flow region is observed behind the capsule. The maximum velocity of the reverse flow is approximately $u \simeq -0.5$. The non-dimensional density inside the recirculating region is $\rho \simeq 0.4$ and the resulting non-dimensional dynamic

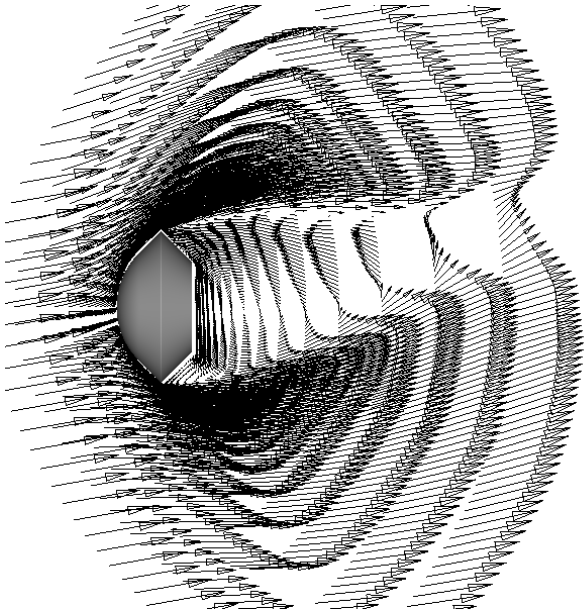

Figure 6.5: Vector map in the plane of symmetry ($\alpha = 10°$,time averaged)

pressure is $\frac{1}{2}\rho u^2 \simeq 0.05$, which is consistent with the height of the pressure peaks in Figs. 6.4(a) and 6.4(b).

Figure 6.6 shows the correlation between the reverse flow and the base pressure. [1] Each picture corresponds to the instance when the pressure peak, indicated by the arrow t1 $\sim$ t6 in Fig. 6.4, appear at the base. The blue semi-transparent surface is the iso-surface of axial velocity $u = -0.4$, which represents the core region of the reverse flow. The color of the surface of the capsule denote the static pressure distribution. The contour of the axial velocity are also plotted at 3 planes, $x = 1.0$, 1.5 and 2.0 to show the position of the reverse flow region within the wake. The contours are displayed only for the subsonic region, and therefore the shape of the contour planes represent the cross sections of the wake at each planes. The high pressure regions at the base (colored yellow and red) always appear at the head of the reverse flow. For the D45 model, the reverse flow passes upper side of the wake and the high pressure spot always appears at the top part of the base. The position of the reverse flow of the D30 model near the base fluctuates with the

[1] Animations are available in the attached CD-ROM. See Appendix D

high pressure spot. These figures indicate that the high pressure spots are caused by the impingement of the reverse flow against the base.

The primary difference between the reverse flow of two capsules is their position at the downstream sections. The reverse flow of the D45 model passes upper side of the wake at all three sections, while the flowfield behind the D30 model is essentially axisymmetric even for the positive pitch angle and the reverse flow passes almost center of the wake at the sections $x = 1.5$ and 2.0. The base pressure distribution of the capsule is considered to be correlated to the flow structure that shifts the reverse flow upward.

6.4 Vortex Structure Behind the Capsule

6.4.1 Time-averaged Streamlines

Figure 6.7 shows the time-averaged streamlines behind the capsules at the fixed pitch angle, $\alpha = 10°$. The two-dimensional time-averaged streamlines in the plane of symmetry are also shown in Fig. 6.8 A pair of large scale vortices is observed behind the D45 model (Fig. 6.7(a)). These vortices are the counterclockwise vortex when observed form the left side (Fig. 6.8(a)), and this vortex pushes the reverse flow upward. The streamlines behind the D30 model (Fig. 6.7(b)) are distorted almost randomly, and no clear flow structure is observed from the figure. In Fig. 6.8(b), the size of the upper vortex (clockwise) and the lower vortex (counterclockwise) are the same, and the flowfield behind the D30 model is almost axisymmetric although the pitch angle of the capsule is not zero.

It becomes clear that the flow structure that makes the wake asymmetric and shifts the reverse flow upward is the pair of vortices behind the capsule.

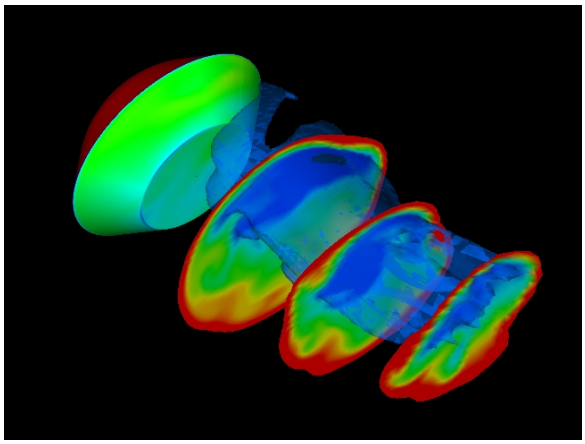

$t = t1$

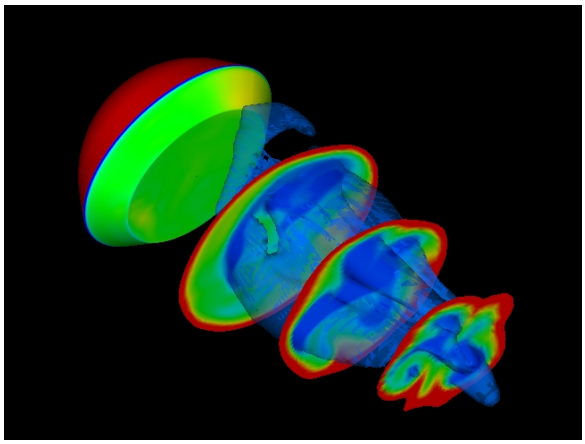

$t = t4$

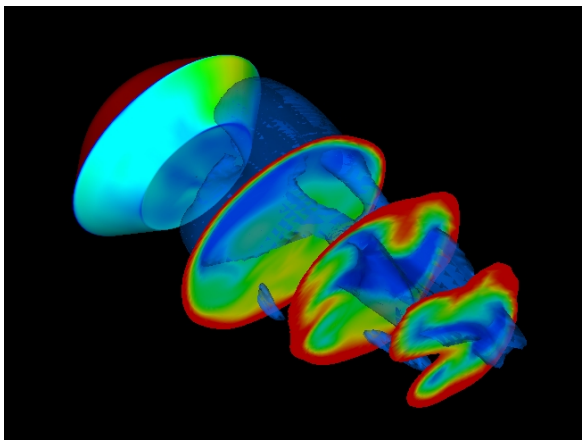

$t = t2$

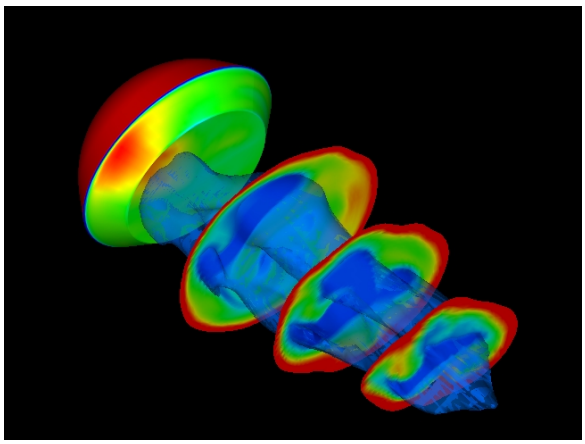

$t = t5$

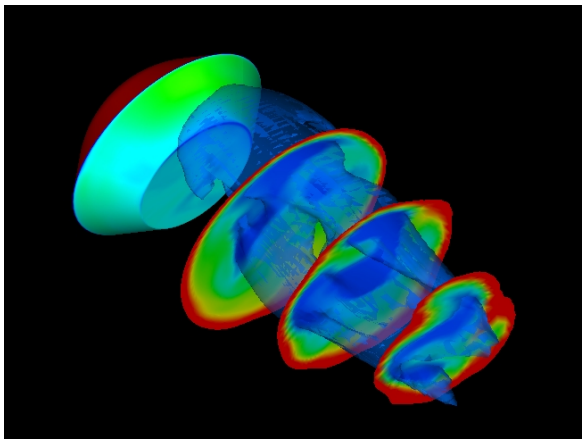

$t = t3$

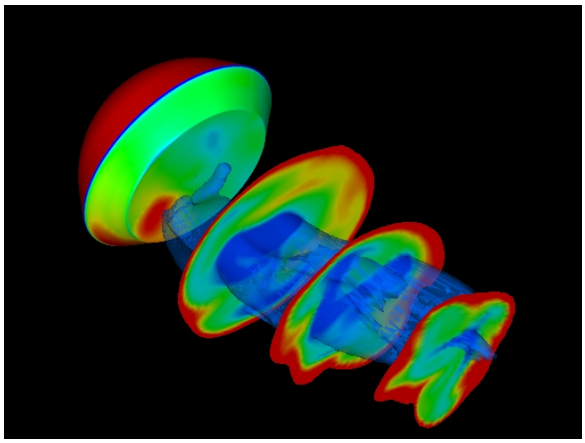

$t = t6$

(a) D45 Model

(b) D30 Model

Figure 6.6: Reverse flow and base pressure ($\alpha = 10°$)

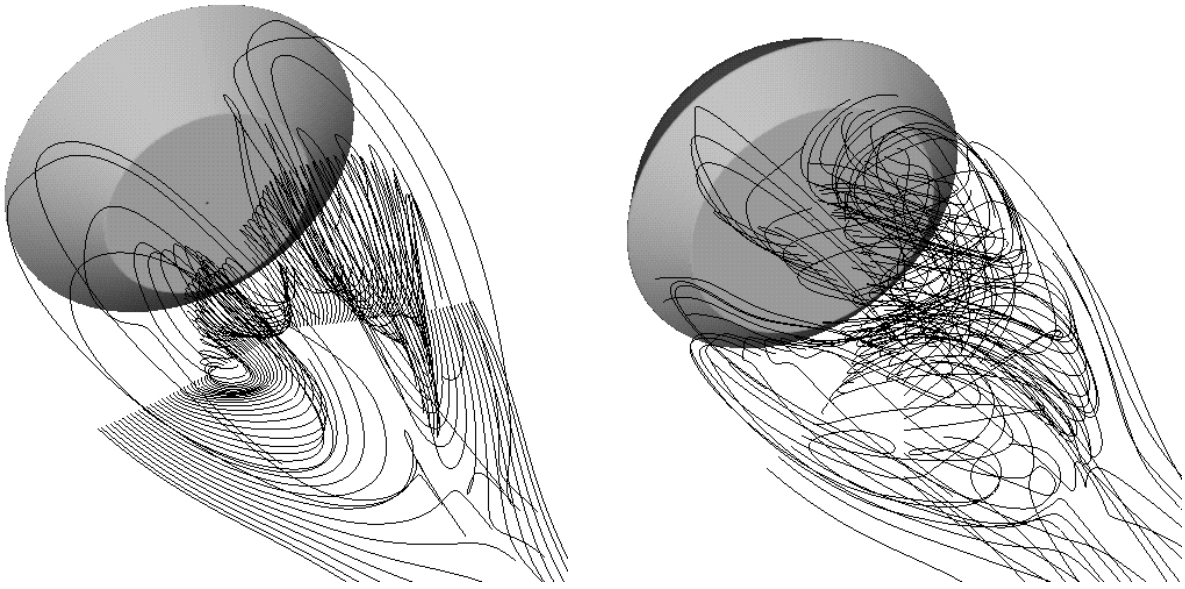

(a) D45 model (b) D30 model

Figure 6.7: Streamlines behind the capsules ($\alpha = 10°$, time-averaged)

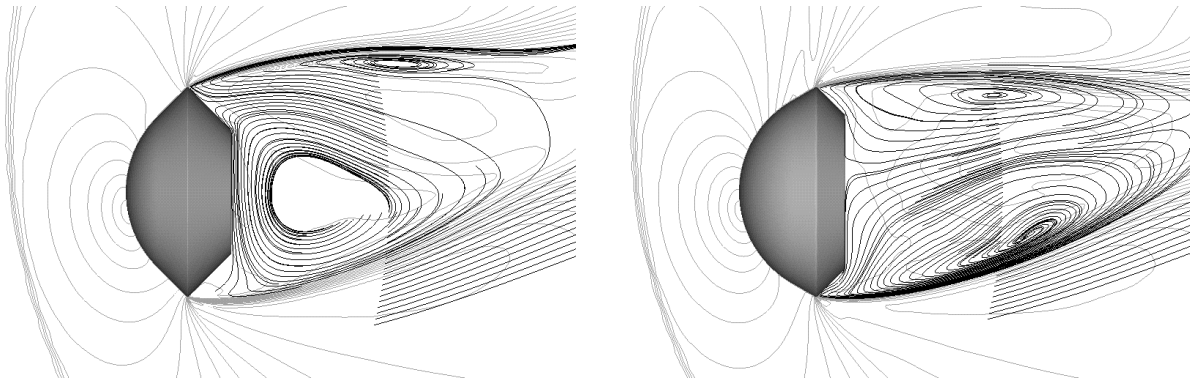

(a) D45 model (b) D30 model

Figure 6.8: Streamlines in the symmetry plane ($\alpha = 10°$, time-averaged)

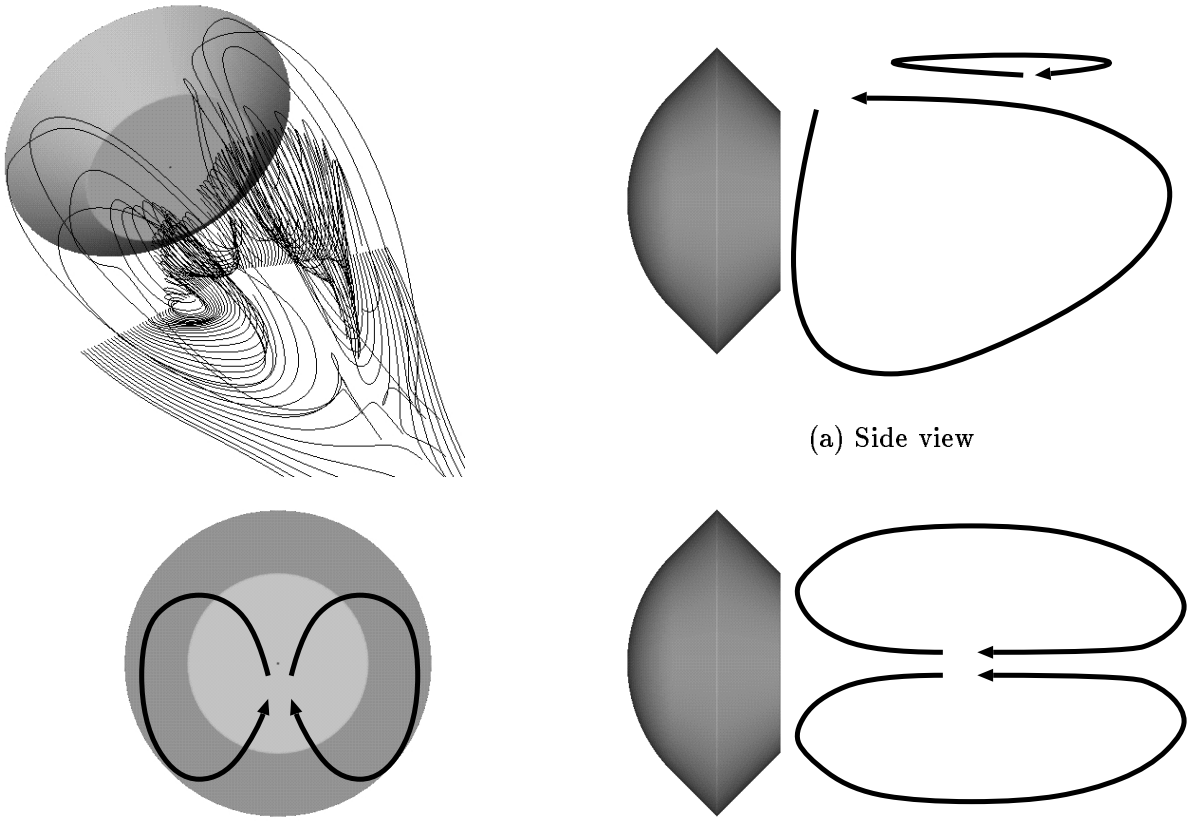

(a) Side view

(b) Back view

(c) Top view

Figure 6.9: Vortex structure behind the D45 model (schematic view)

6.4.2 Vortex behind the Oscillating Capsule

The particle traces behind the D45 model capsule in the forced oscillation are shown in Fig. 6.10. [2] The time series of the physical properties are pre-processed by the LPF with cut-off frequency of 150Hz to eliminate high frequency disturbances. The particles are released from $X/D = 1.25$ in a line at a certain interval, and the unsteady flow structure is visualized by the deformation of the particle line. The color of the particles denotes the residence time after the release, and the color of the capsule show the surface pressure distribution. The capsule is pitching down from $\alpha = 2.73°$ to $\alpha = -14.71°$ in Fig. 6.10.

The large counterclockwise vortex, which is recognized as the region where the particle

[2] Animation is available in the attached CD-ROM. See Appendix D

does not exist, is observed right behind the capsule when the pitch angle is positive (Fig. 6.10(a)). At the moment of Fig. 6.10(b), the pitch angle of the capsule is almost zero. But the counterclockwise vortex is still dominant behind the capsule and the surface pressure at the upper side of the base is higher than the pressure at the lower half. The flowfield behind the capsule is close to that at the small positive pitch angle, and therefore the transition of the flowfield is delayed from the pitch angle of the capsule. As the capsule further pitches down, the counterclockwise vortex gradually diminishes (Fig. 6.10(c)) and a small clockwise vortex is formed at the upper side downstream (Fig. 6.10(e)). It gradually develops and propagates upstream, and finally replace the counterclockwise vortex at the lower side. (Fig. 6.10(g)). The surface pressure at the lower half does not exceeds the pressure at the upper part until the clockwise vortex becomes dominant behind the capsule.

The transition of the base pressure distribution is consistent with the transition of the vortex structure behind the capsule. The base pressure of the capsule in the pitching oscillation is also governed by the vortex structure behind the capsule.

6.4.3 Vortex Core

The vortices behind the capsule have three-dimensional structure. It is difficult to recognize the three-dimensional vortex by two-dimensional pictures of the streamlines (Figs. 6.7 and 6.9), and therefore the behavior of the vortices behind the capsule was discussed only by the two-dimensional streamlines in the plane of symmetry (Figs. 6.8 and 6.10) in the previous two sections. The vortex-core identifying technique developed by Sawada[21] is applied here for the discussion of the three-dimensional structure of the vortices. His method is based on the critical-point analysis, finds out the core of vortices automatically, and visualize the vortices as the locus of the vortex core. It gives more clear view of the vortex structure than the streamlines.

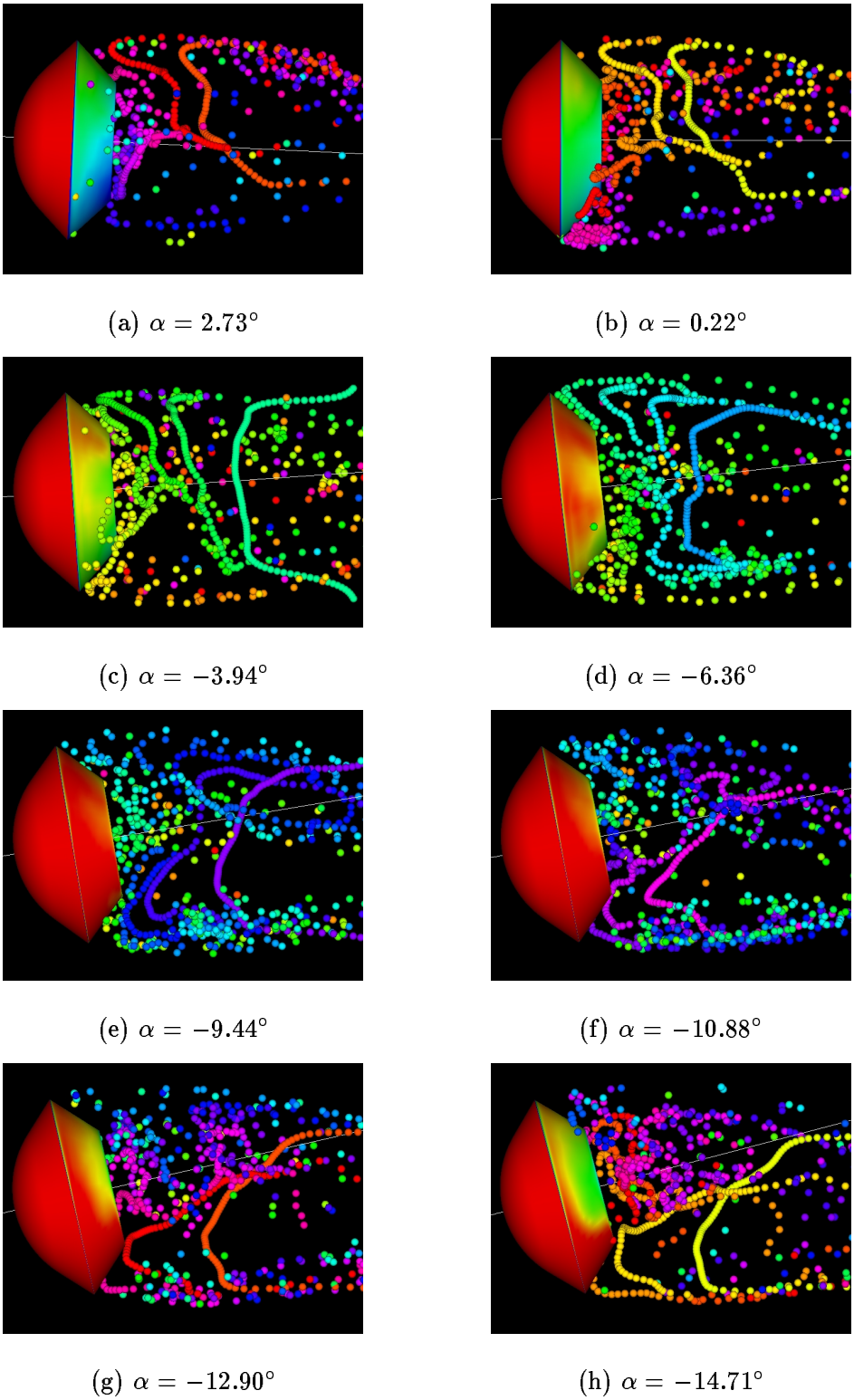

(a) $\alpha = 2.73°$ (b) $\alpha = 0.22°$

(c) $\alpha = -3.94°$ (d) $\alpha = -6.36°$

(e) $\alpha = -9.44°$ (f) $\alpha = -10.88°$

(g) $\alpha = -12.90°$ (h) $\alpha = -14.71°$

Figure 6.10: Particle traces behind the D45 model (Forced pitching oscillation)

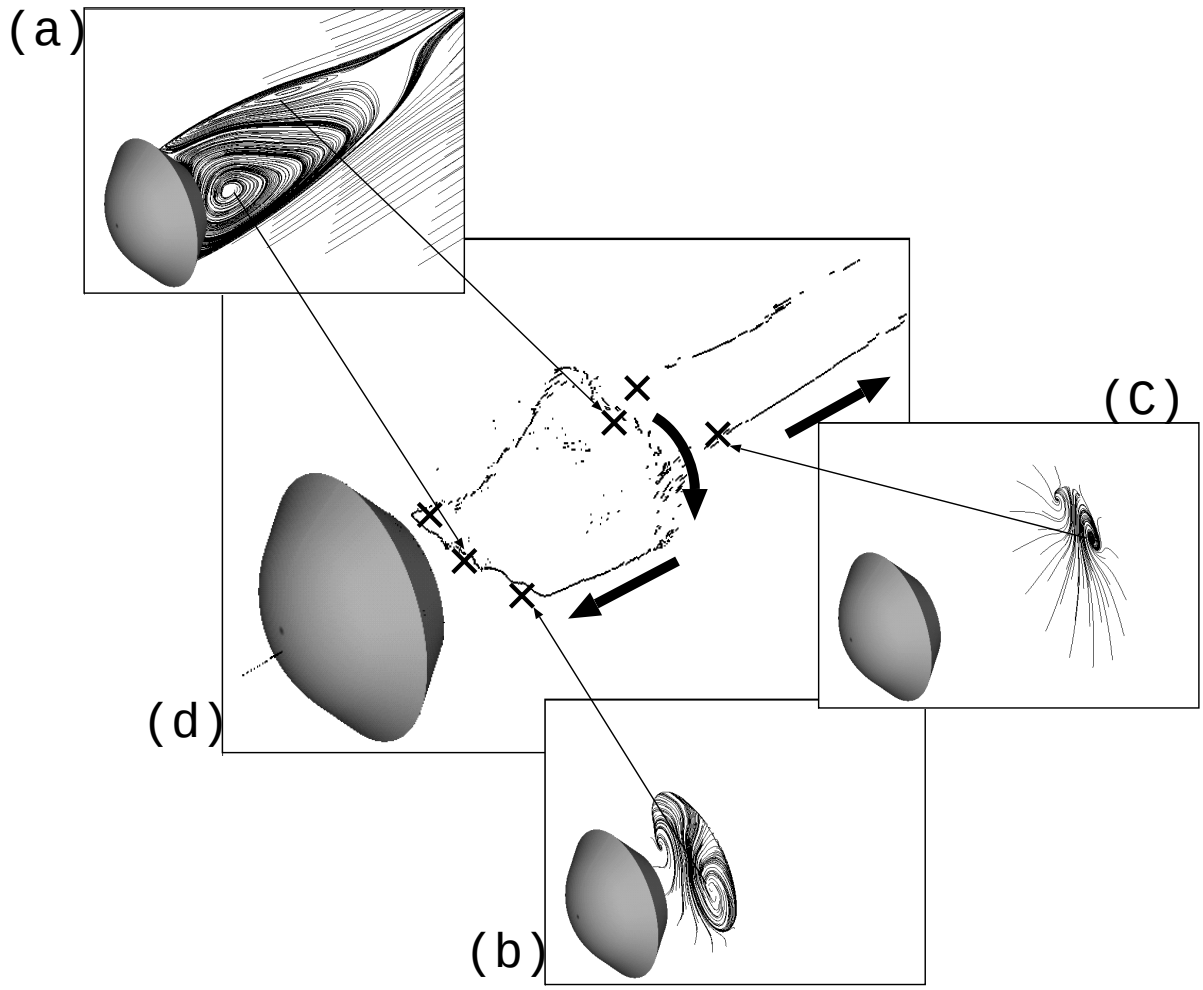

Figure 6.11: Locus of the vortex core ($\alpha = 10°$,time averaged)

Figure 6.11(d) shows the locus of the vortex core behind the D45 model at $\alpha = 10°$, [3] and the arrows in the figure show the direction of the propagation of the vortices. Figures 6.11(a)$\sim$(c) show the two-dimensional streamlines inside each cross section. The vortex behind the capsule is composed of a distorted ring vortex and a pair of longitudinal vortices that emanates from the kink of the ring vortex. The ring vortex corresponds to the reverse flow, as shown in section(a), and two contra-rotating vortices observed in Fig. 6.8 are turned out to be the cross sections of the same ring vortex. The behavior of the reverse flow is correlated to the shape of the ring vortex. That is, when the lower part

[3] Animation is available in the attached CD-ROM. See Appendix D

of the ring vortex is in front of the upper part, the reverse flow directs upward, passes upper side of the wake and hits the base at its upper part.

The vortices at the section (c) are a pair of longitudinal vortices. The right (looking after) vortex rotates clockwise, and the left vortex rotates counterclockwise, and they propagate downstream. The vortices at the section (b) also look like longitudinal vortices, but they are the parts of the distorted ring vortex. The vortex at the section (b) propagates upstream. Although the vortices at the sections (b) and (c) are the separate vortices, they rotates in the same direction, and they both emanate from the neck point. It seems that the vortices at the sections (b) and (c) are both induced by flow structure at the neck point.

Since the vortices at the sections (b) comes from the distortion of the ring vortex, the distortion of the ring vortex, that govern the behavior of the reverse flow, is considered to be closely related to the formation of the longitudinal vortices downstream.

6.4.4 Pair of the longitudinal Vortices

Figure 6.12 shows the sideview of the streamlines inside the shear layer. The streamlines right behind the capsule slightly directs downward. The downward streams converge at the rear end of the recirculating region, roll up, and form upward stream. The rolled up upward stream splits into two streams. The flow going downstream forms the pair of longitudinal vortices, and the flow going upstream distorts the ring vortex. Both the pair of the longitudinal vortices downstream and the distortion of the ring vortex are caused by the roll up of the streamlines inside the shear layer at the neck point.

The streamlines inside the shear layer are directly connected to the pair of the longitudinal vortices downstream, and the streamlines and the longitudinal vortices are considered to be an united flow structure shown in the schematic figure as Fig. 6.13.

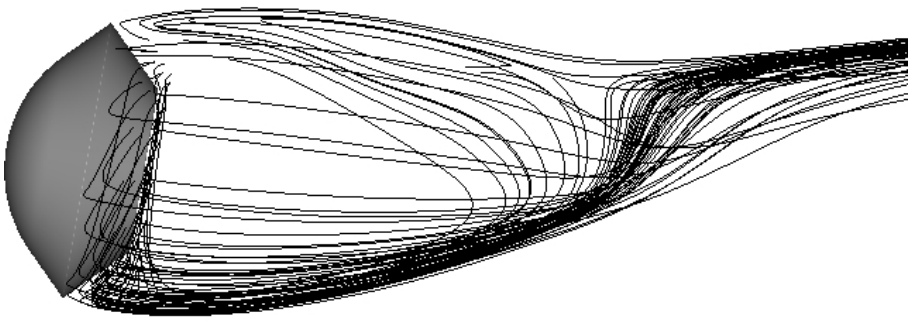

Figure 6.12: Streamlines inside the shear layer ($\alpha = 10°$,time averaged)

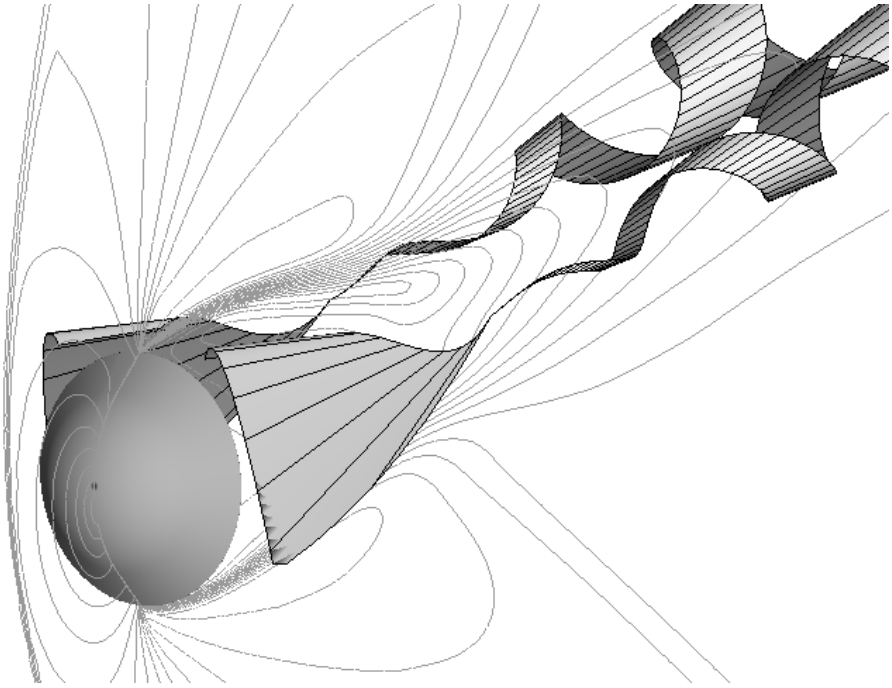

Figure 6.13: Schematic view of the longitudinal vortex pair

6.5 Summary

The flowfields around the capsules at fixed pitch angle are simulated, and the flow structure that controls the base pressure distribution is discussed.

The base pressure distribution is determined by the impingement of the reverse flow against the base. When the reverse flow impinges the base at its top, the upper base pressure becomes higher and the base pressure produce pitch-down moment. The behavior of the reverse flow is correlated to the vortex structure behind the capsule. The vortex behind the capsule is composed of a ring vortex and a pair of longitudinal vortices. It seems that the formation of the pair of longitudinal vortices is closely related to the base pressure distribution.

CHAPTER 7

TOTAL DISCUSSIONS

The flowfield around the capsules has been discussed and the mechanism of the dynamic instability was revealed in the previous chapters. In this chapter, the mechanism of the dynamic instability is summarized, and it is verified through several numerical experiments.

7.1 The Mechanism of the Dynamic Instability

7.1.1 Modeling of the mechanism

The dynamic stability of the capsule is caused by the phase delay of the base pressure. When the pitch angle of the capsule is changed, the base pressure does not change until the information that "the pitch angle has changed" reaches the base through the following four steps. (Fig. 7.1)

When the capsule pitches up from zero angle of attack,

(1) the pressure field at the front side of the capsule changes immediately. The pressure field rotates the flow inside the shear layer behind the capsule downward, and the downward directed flow propagates downstream.

(2) the downward directed flow converges at the rear end of the recirculating region (neck point), rolls up, and forms upward stream. The transition of the flowfield near the neck point is slightly delayed from the motion of the capsule, since the speed

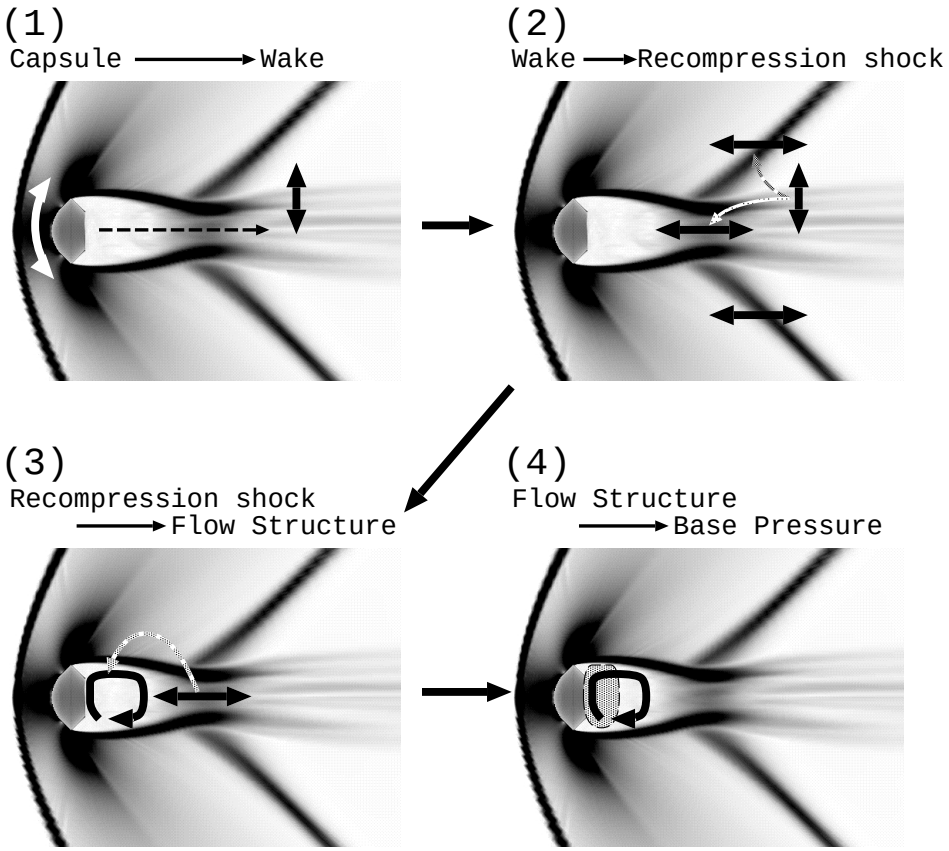

Figure 7.1: The mechanism of the delay of the base pressure

of the propagation inside the shear layer is finite. The motion of the recompression shock wave is coupled with the flowfield near the neck point, and therefore its motion is also delayed.

(3) the rolled up stream induces a pair of longitudinal vortices both upstream and downstream. The upstream longitudinal vortices distorts the ring vortex behind the capsule, and it shifts the reverse flow upward.

(4) the reverse flow impinges the base at its top, and the surface pressure at the upper part of the base becomes higher than the lower part. The base pressure distribution cause pitch-down moment.

These mechanism derive $\delta_b > 0$ and $\left.\frac{\partial M_{b\text{fixed}}}{\partial \alpha}\right|_{\alpha} < 0$. Equation (5.8) tells that the

capsule is dynamically unstable provided $\delta_b \left.\frac{\partial M_{b\text{fixed}}}{\partial \alpha}\right|_\alpha < 0$, and therefore the capsule becomes dynamically unstable until certain pitch angle is reached.

7.1.2 Limitation of the model mechanism

The model mechanism well describes the features observed in the numerical results. However, the present model should not be applied to all the reentry capsules. The present model is based on the following two conditions, and therefore the present model should be applied only to the capsule that satisfies these conditions:

(1) the flowfield behind the capsule is characterized by the reverse flow, and the behavior of the reverse flow is correlated to the vortex structure behind the capsule

(2) the base pressure causes pitch-down moment when the pitch angle is positive

The vortex behind the capsule studied in this thesis is composed of a ring vortex and a pair of the longitudinal vortices. The ring vortex is formed by the separation at the edge of the capsule. Suppose that the capsule had a cylindrical body, the flow would separate at the side surface of the body rather than the edge of the base surface when the angle of attack is not zero. The separation at the side surface forms a pair of longitudinal vortices instead of a ring vortex, and the vortex structure behind the capsule would be different from that assumed in the modeling. Therefore the first condition requires that the capsule has no or very short cylindrical body.

If the vortex structure behind the capsule is same as that of the capsule studied in this thesis, the pressure at the upper part of the base becomes higher when the pitch angle is positive. The high pressure region at the upper part produces pitch-down moment when the normal vector of the high pressure region cross the axis of symmetry forward of the center of the gravity of the capsule (Fig.7.2). Therefore the second condition requires that the base part of the capsule has large semi-apex angle and that it is nearly flat.

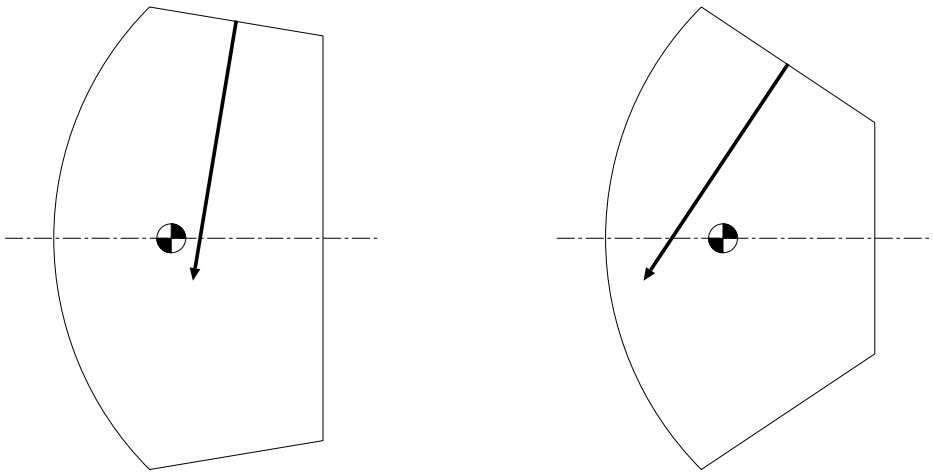

pitch-up moment pitch-down moment

Figure 7.2: Base configuration and the pitching moment

7.2 Numerical Experiments

Two hypothesis are deduced from the mechanism described in the previous section.

- **the phase delay angle ϕ is proportional to the frequency of the oscillation**

  The delay of the base pressure is caused by the propagation of the downward directed flow from the capsule to the neck point. The speed of the propagation and the distance between the capsule and the neck point do not change with the frequency of the oscillation, and therefore the delay time is constant regardless of the frequency. The phase angle ϕ is given by $\phi = 2\pi f\delta$, and the delay phase angle should be proportional to the frequency f.

  In other words, the phase delay angle is proportional to the size of the capsule, so long as the frequency of the oscillation is kept constant. If the capsule is scaled up twice, the distance between the capsule and the neck point also becomes twice. The time required to for the disturbance to propagate becomes double, and the resulting phase delay angle is also double of that of the original capsule.

- **the dynamic stability of a capsule depends mainly on its forebody shape**

frequency	average pressure	amplitude	phase angle
20 Hz	0.3163	0.03604	-16.4 deg
40 Hz	0.3141	0.03495	-29.4 deg

Table 7.1: Characteristics of the base pressure oscillation for different frequency

$\frac{\partial M_{b\text{fixed}}}{\partial \alpha}$ is governed by the characteristics of the base pressure distribution. The base pressure distribution is correlated to the downward directed flow behind the capsule, and the downward directed flow is considered to be influenced by the pressure field outside of the wake. Since the pressure field outside of the wake depends mainly on the forebody shape of the capsule, the dynamic stability of a capsule depends mainly on the forebody shape.

Additional simulations are carried out to verify these hypothesis.

7.2.1 Oscillation with Higher Frequency

The flowfield around the D45 model under the forced pitching oscillation is simulated. The numerical conditions and the grid are same as those in chapter 4 but for the different frequency of the oscillation. This time, the frequency of the forced oscillation is 40Hz, which is double of that in chapter 4.

The time history of the surface pressure at one point at the base is shown in Fig. 7.3, and the characteristic parameters of the pressure oscillation are compared with those for the oscillation of 20Hz in the Table 7.1. The time averaged pressure and the amplitude of the oscillation is almost same for two frequencies, while the phase angle for the 40Hz is approximately double of that for the 20Hz The delay phase angle is proportional to the frequency of the oscillation, and the result supports the hypothesis.

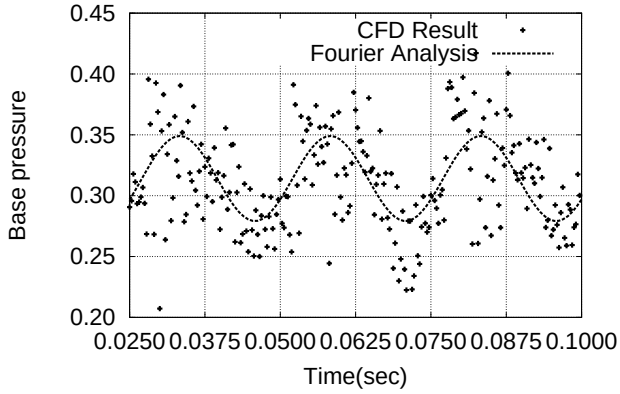

Figure 7.3: Time history of the base pressure (f =40Hz)

7.2.2 Parametric Study about the Shape of the Capsule

The evaluation of the dynamic stability requires the simulation of the oscillating capsule, and it is too expensive for the parametric study. Therefore, the flowfields around miscellaneous capsules at fixed pitch angle are simulated and the flowfields behind the capsule, which are directly coupled with their dynamic stability, are compared. Three capsules shown in the bottom of Fig. 7.4 are all composed of the forebody and the afterbody of the D45 and the D30 models. The D45flt model is the forebody of the D45 model with flat base, the D45+30 model is composed of the forebody of the D45 model and afterbody of the D30 model, and the D30+45 model is the combination of the afterbody of the D45 model and forebody of the D30 model.

Figures 7.5 and 7.6 show the time-averaged base pressure distributions in the plane of symmetry of these capsules, at the angle of attack $\alpha = 10°$. The base pressure of capsules which have D30 forebody are almost uniform, while the base pressure of all the capsules with D45 forebody become higher at the leeward side (upper part). Although the height and the extent of the high pressure region changes with the afterbody shape, base pressure distribution seems to be determined mainly by the forebody configuration. The characteristic of the time-averaged streamlines (Fig.7.7) also depends mainly on the

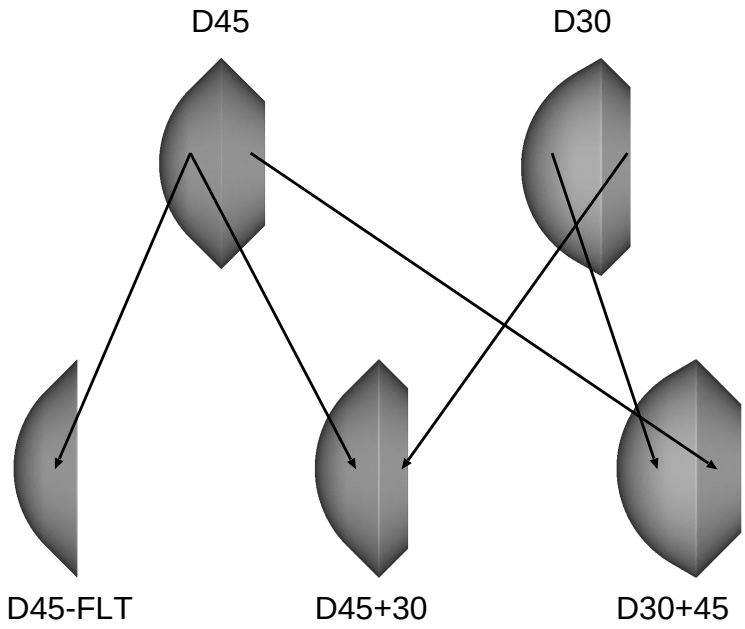

Figure 7.4: Capsules composed of forebody & afterbody of D45 & D30 models

forebody configuration. The pair of longitudinal vortices is observed only behind the capsules with the D45 forebody, and not behind the capsules with the D30 forebody. Influence of the afterbody configuration on the formation of the longitudinal vortex pair seems to be small.

These results indicate that base pressure distribution of a capsule, and therefore the dynamic stability of a capsule principally depends on the forebody configuration. Berner[8] and Hiraki[22] both reported from their experiments that small modifications in the base geometry do not affect the dynamic stability of the capsule, which supports the above hypothesis.

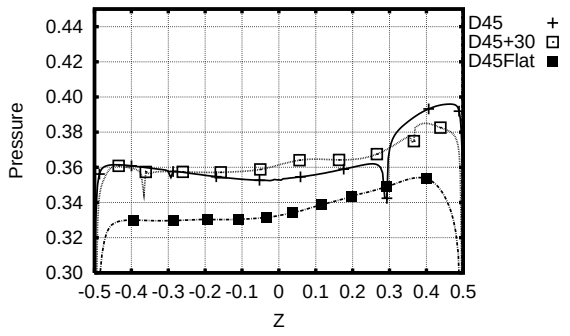

Figure 7.5: Time averaged base pressure (D45 forebody)

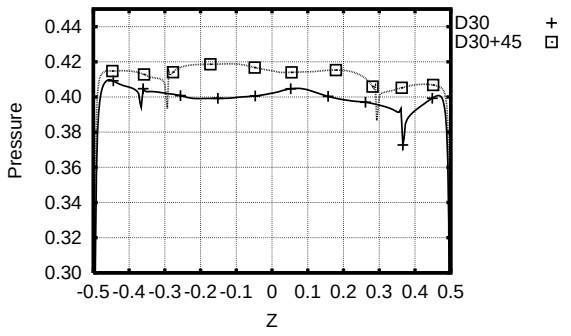

Figure 7.6: Time averaged base pressure (D30 forebody)

7.3 Shape of the Capsule and Its Aerodynamic Characteristics

The discussions in the previous chapter indicate that $\frac{\partial M_b}{\partial \alpha}_{\text{fixed}}$ is closely related to the formation of the pair of longitudinal vortices shown in Fig. 6.13. The vortices are analogous to the "tip vortex" of a wing. The most simplified expression of the circulation Γ of the tip vortex is

$$\begin{aligned} L &= \frac{1}{2}\rho V^2 C_L S = \rho V \Gamma b \\ \Gamma &= \frac{1}{2} V a C_L \end{aligned} \tag{7.1}$$

The strength of the tip vortex is proportional to the lift coefficient C_L. Analogously, the dynamic stability of the capsule, which is coupled with the strength of the longitudinal vortices, may also be related to the static lift coefficient of the capsule. Figure 7.8 shows the lift coefficient of the D45 model and the D30 model. Only the D45 model is dynamically unstable, and $|C_{L\alpha}|$ of the D45 model is far larger than that of the D30 model.

It is impossible to draw a conclusion from only one example, but it seems that the capsule with large $|C_{L\alpha}|$ tends to be dynamically unstable.

7.4 Summary

The detailed mechanism of the dynamic instability of the capsule is discussed. The phase delay of the base pressure is created through the feedback-loop from the capsule, wake, recompression shock wave, and to the base pressure. Then the delay of the base pressure makes the capsule dynamically unstable. The mechanism well describes the features observed in the results in the previous chapters. This model can be applied to the capsule without no or very short cylindrical body and nearly flat base. Additional numerical simulations are carried out to verify the hypothesis derived from the mechanism, and the results are consistent with the hypothesis.

The correlation between static and dynamic aerodynamic coefficients are discussed. It seems that the capsule with large $|C_{L\alpha}|$ tends to be dynamically unstable.

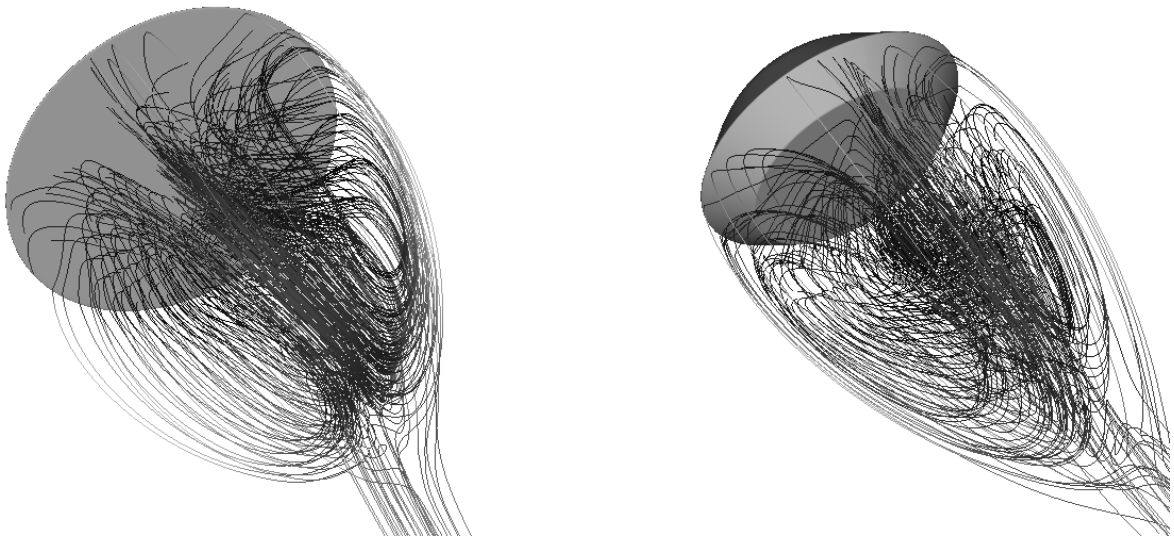

(a) D45flt

(b) D45+30

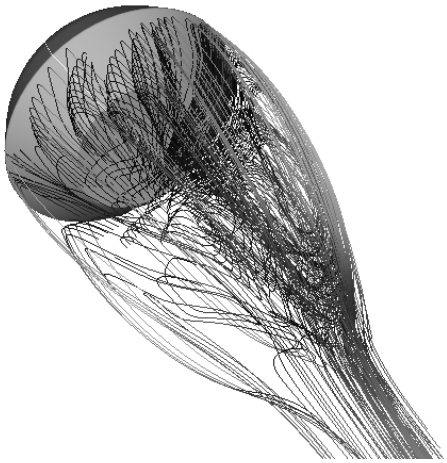

(c) D30+45

Figure 7.7: Time averaged streamline for miscellaneous capsules

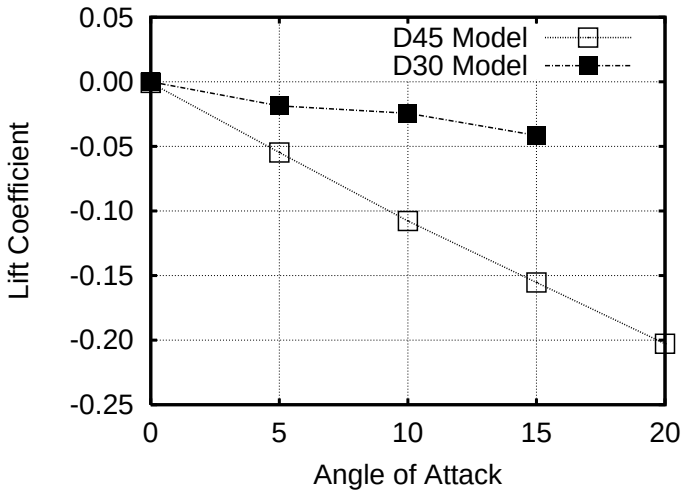

Figure 7.8: Lift Coefficient for D45 & D30 model

CHAPTER 8

CONCLUDING REMARKS

The flowfield around the blunt capsules, that represent the reentry capsule used in the sample-return project, are numerically studied for the better understanding of the mechanism of the dynamic instability of the capsule at transonic speeds.

The flowfield around the capsule in the forced pitching oscillation was numerically simulated. The results indicated that the oscillation of the base pressure is slightly delayed from that of the pitch angle, while the foreside surface pressure varies synchronously with the pitch angle. The base pressure, the recompression shock wave, and the wake near the neck point all oscillate with the same delay time, and the oscillation of the base pressure is considered to be coupled with the flowfield around the neck point.

The flowfield around the capsule at fixed pitch angle were compared with the flowfield around the capsule in the oscillation. The characteristics of the surface pressure for two flowfield are turned out to be essentially the same except for the slight delay in the base. The surface pressure of the oscillating capsule was modeled by a simple constant-delay model, and the dynamic stability of the capsule was discussed based on the model. It was shown that the dynamic stability of the capsule depends mainly on the behavior of the base pressure. The capsule is dynamically unstable provided that the base pressure produce pitch-down moment for the positive pitch angle, and the transition of the base pressure is delayed from the pitch angle.

The characteristic of the base pressure was discussed from the simulation of the flowfield around the capsule at fixed pitch angles. There is strong reverse flow behind the

capsule, and the impingement of the reverse flow against the base determine the base pressure distribution. The flowfield behind the capsule is characterized by the vortex that is composed of a ring vortex and a pair of longitudinal vortices. The longitudinal vortices induce upward stream at the neck point when the capsule pitches up, and the upward stream push the reverse flow upward, and the base pressure produce pitch down moment. The base pressure does not changes, when the pitch angle of the capsule changes, until the change of the longitudinal vortices caused by the attitude change propagates downstream and reaches the neck point. The time lag causes the phase delay of the base pressure.

Both the base pressure distribution and its delay are closely related to the pair of the longitudinal vortices, and therefore the dynamic stability of the capsule is considered to be related to the formation of the pair of the longitudinal vortices downstream.

The mechanism of the dynamic instability revealed in this study reasonably explains all the characteristic features observed in the numerical simulations. It is also consistent with several important features reported in the former experiments.

BIBLIOGRAPHY

[1] K. Hiraki, Y. Inatani, N. Ishii, T. Nakajima, and M. Hinada, "Dynamic stability of MUSES-C capsule," in *21st International Symposium on Space Technology and Science*, May 1998. ISTS-98-d-33.

[2] Working group of Asteroid Sample Return Mission, *Asteroid Exploration Plan (Muses-C)*. The Institute of Space and Astronautical Science, Mar. 1995. (in Japanese).

[3] B. R. Wright and R. A. Kilgore, "Aerodynamic damping and oscillatory stability in pitch and yaw of Gemini configurations at Mach numbers from 0.50 to 4.63," NASA Technical Note NASA TN D-3334, Mar. 1966.

[4] M. V. Krumins, "Drag and stability of Mars probe/lander shapes," *Journal of Spacecraft*, vol. 4, no. 8, pp. 1052–1057, 1967.

[5] R. I. Sammonds, "Dynamics of high-drag probe shapes at transonic speeds," NASA Technical Note NASA TN D-6489, Sept. 1971.

[6] R. I. Sammonds and R. L. Kruse, "Viking entry vehicle aerodynamics at M=2 in air and some preliminary test data for flight in CO_2 at M=11," NASA Technical Note NASA TN D-7974, June 1975.

[7] T. Yoshinaga, A. Tate, M. Watanabe, and T. Shimoda, "Orbital re-entry experiment vehicle ground and flight dynamic test results comparison," *Journal of Spacecraft and Rockets*, vol. 33, no. 5, pp. 635–642, 1996.

[8] C. Berner and G. L. Winchenbach, "A numerical and experimental investigation of generic space probes," AIAA Paper 98-0798, Jan. 1998.

[9] G. T. Chapman and L. A. Yates, "Dynamics of planetary probes: Design and testing issues," AIAA Paper 98-0797, Jan. 1998.

[10] G. T. Chapman, R. A. Mitcheltree, and W. H. Hathaway, "Transonic and low subsonic static and dynamic aerodynamic characteristics of the Stardust sample return capsule," AIAA Paper 99-1021, 1999.

[11] M. Tobak, L. B. Schiff, and V. L. Peterson, "Aerodynamics of bodies of revolution in coning motion," *AIAA Journal*, vol. 7, no. 1, pp. 95–99, 1969.

[12] M. Tobak and W. E. Pearson, "A study of nonlinear longitudinal dynamic stability," NASA Technical Report NASA TR R-209, Sept. 1964.

[13] P. L. Roe, "Approximate Riemann solvers, parameter vectors, and difference schemes," *Journal of Computational Physics*, vol. 43, pp. 357–372, 1981.

[14] E. Shima and T. Jounouchi, "Role of CFD in aeronautical engineering (No.14) - AUSM type upwind schemes -," in *Proceedings of the 14th NAL Symposium on Aircraft Computational Aerodynamics*, pp. 7–12, 1997.

[15] M. S. Liou and C. J. Steffen Jr, "A new flux splitting scheme," *Journal of Computational Physics*, vol. 107, pp. 23–39, 1993.

[16] W. K. Anderson, J. L. Thomas, and B. Van Leer, "Comparison of finite volume flux vector splitting for the euler equations," *AIAA Journal*, vol. 24, no. 9, pp. 1453–1460, 1986.

[17] S. Obayashi, K. Matsushima, K. Fujii, and K. Kuwahara, "Improvements in efficiency and reliability for navier-stokes computations using the LU-ADI factorization algorithm," AIAA Paper 86-0338, Jan. 1986.

[18] K. Imai and K. Fujii, "Effect of the time step size in the implicit algorithm for unsteady simulation," in *Proceedings of 1999 JSME Annual Meeting*, vol. 2, pp. 81–82, July 1999. (In Japanese).

[19] B. S. Baldwin and H. Lomax, "Thin layer approximation and algebraic model for turbulent flows," AIAA Paper 78-257, Jan. 1978.

[20] R. Kuc, *Introduction to Digital Signal Processing*. New York: McGraw-Hill, 1982.

[21] K. Sawada, "A convenient visualization method for identifying vortex cores," *Trans. Japan Soc. Aero. Space Sci.*, vol. 38, no. 120, pp. 102–120, 1995.

[22] K. Hiraki, *Experimental Investigation of the Dynamic Instability of Capsule-shaped Objects*. PhD thesis, The University of Tokyo, 1998. (In Japanese).

APPENDIX A

NAVIER-STOKES EQUATIONS

The conservation form of the three-dimensional Navier-Stokes equations written in the cartesian coordinate system are as follows

$$\frac{\partial Q}{\partial t} + \frac{\partial E}{\partial x} + \frac{\partial F}{\partial y} + \frac{\partial G}{\partial z} = \frac{1}{Re}\left(\frac{\partial E_v}{\partial x} + \frac{\partial F_v}{\partial y} + \frac{\partial G_v}{\partial z}\right) \tag{A.1}$$

$$Q = \begin{bmatrix} \rho \\ \rho u \\ \rho v \\ \rho w \\ e \end{bmatrix}, \quad E = \begin{bmatrix} \rho u \\ \rho u^2 + p \\ \rho uv \\ \rho uw \\ (e+p)u \end{bmatrix}, \quad F = \begin{bmatrix} \rho v \\ \rho vu \\ \rho v^2 + p \\ \rho vw \\ (e+p)v \end{bmatrix}, \quad G = \begin{bmatrix} \rho w \\ \rho wu \\ \rho wv \\ \rho w^2 + p \\ (e+p)w \end{bmatrix}$$

$$E_v = \begin{bmatrix} 0 \\ \tau_{xx} \\ \tau_{xy} \\ \tau_{xz} \\ \beta_x \end{bmatrix}, \qquad F_v = \begin{bmatrix} 0 \\ \tau_{yx} \\ \tau_{yy} \\ \tau_{yz} \\ \beta_y \end{bmatrix}, \qquad G_v = \begin{bmatrix} 0 \\ \tau_{zx} \\ \tau_{zy} \\ \tau_{zz} \\ \beta_z \end{bmatrix}$$

Static pressure p is evaluated from the equation of state of the ideal gas

$$p = (\gamma - 1)\left\{e - \frac{1}{2}\rho(u^2 + v^2 + w^2)\right\} \tag{A.2}$$

The stress tensor τ and the heat flux vector β are given as

$$\begin{aligned}
\tau_{xx} &= -\frac{2}{3}\mu(u_x + v_y + w_z) + 2\mu u_x \\
\tau_{yy} &= -\frac{2}{3}\mu(v_y + w_z + u_x) + 2\mu u_y \\
\tau_{zz} &= -\frac{2}{3}\mu(w_z + u_x + v_y) + 2\mu u_z
\end{aligned}$$

$$\tau_{xy} = \tau_{yx} = \mu(u_y + v_x), \qquad \tau_{xz} = \tau_{zx} = \mu(w_x + u_z), \qquad \tau_{yz} = \tau_{zy} = \mu(v_z + w_y)$$

$$\begin{aligned}
\beta_x &= u\tau_{xx} + v\tau_{xy} + w\tau_{xz} + \frac{\mu}{Pr(\gamma - 1)}(c^2)_x \\
\beta_y &= u\tau_{yx} + v\tau_{yy} + w\tau_{yz} + \frac{\mu}{Pr(\gamma - 1)}(c^2)_y \\
\beta_z &= u\tau_{zx} + v\tau_{zy} + w\tau_{zz} + \frac{\mu}{Pr(\gamma - 1)}(c^2)_z
\end{aligned}$$

The effect of the turbulence is simulated as the eddy viscosity, and the molecular viscosity coefficient μ and the Prandtl number Pr in the stress terms are replaced by

$$\mu = \mu_l + \mu_t, \qquad \frac{\mu}{Pr} = \frac{\mu_l}{Pr_l} + \frac{\mu_t}{Pr_t}$$

for the turbulent simulation.

The physical properties are non-dimensionalized by the density and the speed of sound of the free stream, and the characteristics length.

$$\rho = \frac{\rho^*}{\rho^*_\infty}, \quad u = \frac{u^*}{c^*_\infty}, \quad v = \frac{v^*}{c^*_\infty}, \quad w = \frac{w^*}{c^*_\infty}, \quad p = \frac{p^*}{\rho^*_\infty {c^*_\infty}^2} = \frac{p^*}{\gamma p^*_\infty}$$

$$x = \frac{x^*}{L^*}, \quad y = \frac{y^*}{L^*}, \quad z = \frac{z^*}{L^*}, \quad t = \frac{t^*}{L^*/c^*_\infty}, \quad \mu = \frac{\mu^*}{\mu^*_\infty}$$

where the superscript $*$ denotes dimensional value, and the subscript ∞ denotes free stream conditions. The Reynolds number is given as

$$Re = \frac{\rho^*_\infty c^*_\infty L^*_\infty}{\mu^*_\infty} = \frac{1}{M_\infty} \frac{\rho^*_\infty u^*_\infty L^*_\infty}{\mu^*_\infty}$$

APPENDIX B

TEMPORAL ACCURACY OF THE LU-ADI METHOD

Imai studied the shedding of the Karman vortex behind the two-dimensional cylinder using the LU-ADI factorized implicit method, and discussed the temporal accuracy of the LU-ADI method. [18] The basic equations are the thin-layer two-dimensional Navier-Stokes equations. The numerical fluxes are evaluated by the SHUS scheme, and the first order Euler implicit scheme ($\lambda = 1$) is used for the time integration. These numerical methods are same as those described in chapter 3, except for the dimension of the basic equations. Imai carried out series of the simulations using following two implicit schemes for several the time step Δt, and the flowfield and the Strouhal number $St = fD/u$ are compared.

- **the LU-ADI without inner iteration**

  the implicit scheme same as that used in the present dissertation. The scheme contains error due to the linearization, the factorization and diagonalization and the temporal accuracy of the scheme is less than first order.

- **the LU-ADI with inner iteration**

  the error due to the linearization etc. are eliminated by the Newton-Raphson iteration. The temporal accuracy of this scheme is exactly first order.

The Strouhal number St is plotted against Δt in Fig. B.1. The Strouhal number

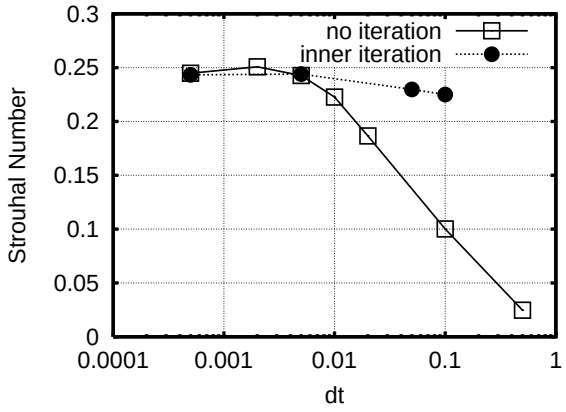

Figure B.1: Strouhal number

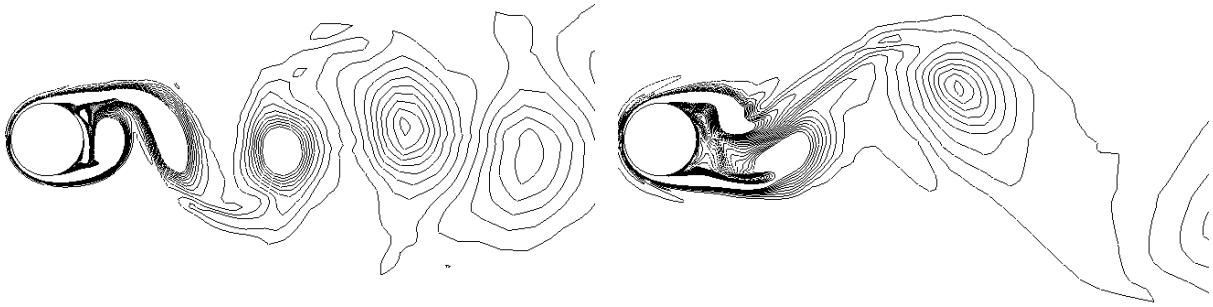

(a) $\Delta t = 0.005$ (b) $\Delta t = 0.1$

Figure B.2: Instantaneous vorticity distribution around the cylinder

evaluated from two different schemes converge to the same value for $\Delta t < 0.005$. The LU-ADI method without inner iteration is considered to be accurate enough to resolve the unsteady evolution of the flowfield with $\Delta t < 0.005$.

Figures B.2(a),B.2(b) show the instantaneous flowfield simulated by the LU-ADI method without inner iteration for two values of Δt. The Karman vortices start growing at the shear layer right behind the cylinder for $\Delta t = 0.005$, while the growth of the vortices is relatively slow for $\Delta t = 0.1$, and the difference in the initial growth of the vortices cause the difference in the spacing of the vortices downstream. Therefore, it seems that

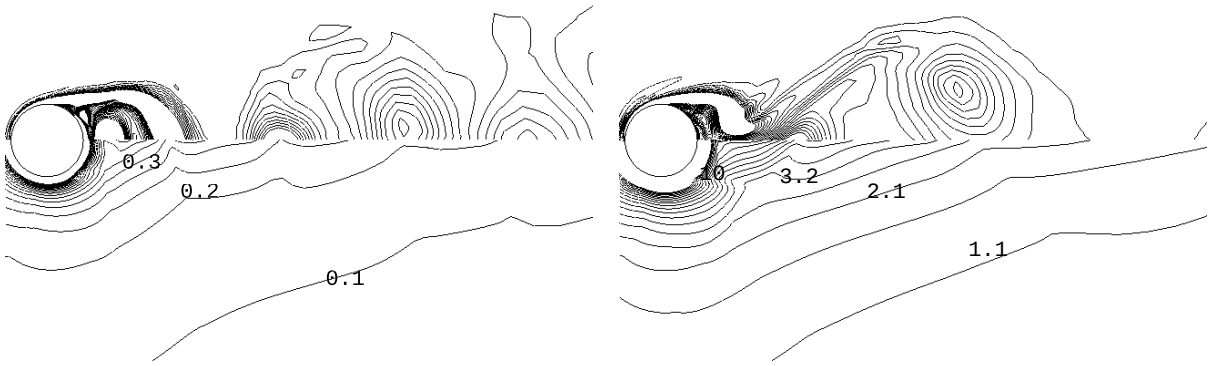

(a) $\Delta t = 0.005$ (b) $\Delta t = 0.1$

Figure B.3: Top:Vorticity , Bottom: Courant number

the temporal accuracy at the region where the vortices start growing is important to evaluate the unsteady behavior of the entire flowfield.

Figures B.3(a),B.3(b) show the local Courant number distribution. The contour lines of the vorticity is plotted in the top half for reference. The local Courant number at edge of the boundary layer where the vortices start growing is $O(10)$ for $\Delta t = 0.1$ and $O(1)$ for $\Delta t = 0.005$.

The LU-ADI method is considered to has enough temporal accuracy to resolve the behavior of large scale vortex structure provided that the local CFL number is smaller than unity.

APPENDIX C

COMPARISON WITH HIRAKI'S EXPRESSION

Hiraki[22] expressed the aerodynamic pitching moment as a function of pitch angle θ and the pitch angular velocity $\dot{\theta}$ as follows

$$M = I\dot{\theta} = qSd \cdot C_m(\theta, \dot{\theta}) \tag{C.1}$$

Equation (C.1) is expanded into Taylor series around $\dot{\theta} = 0$, and the terms higher than second order are omitted

$$\begin{aligned} C_m(\theta, \dot{\theta}) &= C_m(\theta, \dot{\theta} = 0) + \left.\frac{\partial C_m}{\partial \dot{\theta}}\right|_{\dot{\theta}=0} \cdot \left(\frac{d}{V}\right)\dot{\theta} \\ &= C_{mst}(\theta) + C_{m\dot{\theta}}(\theta) \cdot \left(\frac{d}{V}\right)\dot{\theta} \end{aligned} \tag{C.2}$$

where C_{mst} is the static pitch moment coefficient, and $C_{m\dot{\theta}}$ is the pitch damping coefficient. Hiraki expressed these coefficients as follows

$$C_{mst} = a \cdot \theta + b \cdot \theta^3 \tag{C.3}$$

$$C_{m\dot{\theta}} = \varepsilon\left(1 - \frac{\theta^2}{\delta^2}\right) \tag{C.4}$$

where $a, b, \varepsilon, \delta$ are the constants. He identified these constants from his experimental

results using curve-fit technique, and showed that the time history of the pitch angle predicted from these equations are coincident with the experimental results. He also found that the amplitude of the limit cycle oscillation of the larger capsule is also consistent with the prediction with the same constants $a, b, \varepsilon, \delta$, and concluded that the constant δ does not depends on the scale and the inertia moment of the capsule or the free stream conditions.

Substituting Eq. (C.2) into Eq. (C.1) and compare with Eq. (5.5), it reveals that

$$-\delta_b \left. \frac{\partial M_{b\text{fixed}}}{\partial \alpha} \right|_\alpha \tag{C.5}$$

in the present study corresponds to

$$qSd \cdot C_{m\dot{\theta}} = qSd \cdot \varepsilon \left(1 - \frac{\theta^2}{\delta^2}\right) \tag{C.6}$$

in Hiraki's expression.

$M_{b\text{fixed}}$ is approximated by Eq. (5.9), and Eq. (C.5) yields

$$-\delta_b \left. \frac{\partial M_{b\text{fixed}}}{\partial \alpha} \right|_\alpha = \begin{cases} -\delta_b a_M b_M \left(1 - \tanh^2\left(b_M \alpha\right)\right) & |\alpha| < \alpha_{M0} \\ -\delta_b a_M b_M \left(1 - \tanh^2\left(b_M \alpha_{M0}\right)\right) & |\alpha| > \alpha_{M0} \end{cases} \tag{C.7}$$

$$a_M = -0.0019, \quad b_M = 0.5, \quad \alpha_{M0} = 5.5$$

Figures C.1 and C.2 show the Eq. (C.5) and Eq. (C.6), plotted for several δ_b and ε respectively.

Both Eq. (C.5) and Eq. (C.6) linearly increases with δ_b and ε at small $|\alpha|$ where the capsule becomes dynamically instability, It indicates that ε in Hiraki's expression corresponds to the delay time δ_b in the present study.

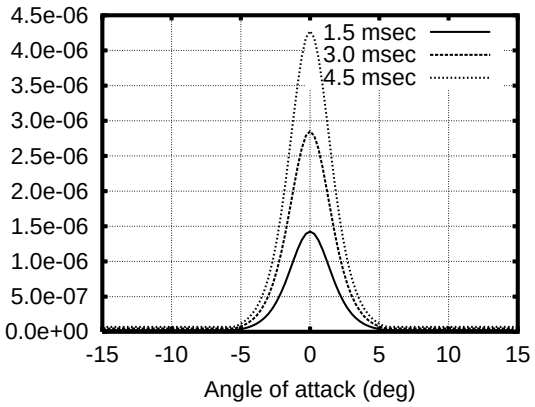

Figure C.1: Equation (C.5)

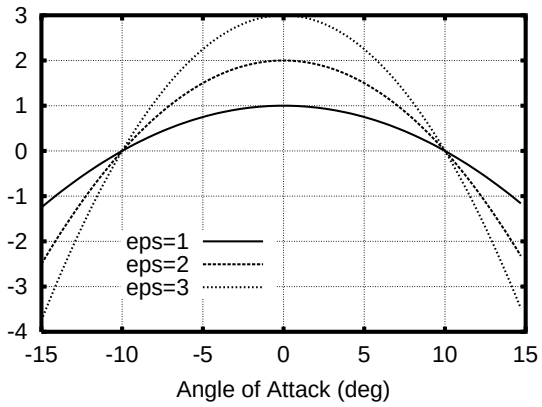

Figure C.2: Equation (C.6)

APPENDIX D

MOVIE FILES IN THE CD-ROM

Following MPEG-1 movies are recorded in the attached CD-ROM.

- **oscillate-capsule_s.mpg** (Fig. 4.4)

  Density gradient around the oscillating D45 model capsule

- **mu45.mpg** (Fig. 6.6(a))

  correlation between the reverse flow and the base pressure of the D45 capsule

- **mu30.mpg** (Fig. 6.6(b))

  correlation between the reverse flow and the base pressure of the D30 capsule

- **particle.mpg** (Fig. 6.10)

  particle traces behind the oscillating D45 model capsule

- **vcore-stdy45_4.mpg** (Fig. 6.11(d))

  locus of the vortex core behind the D45 capsule at $\alpha = 10°$